Supplementary Information

An electrochemically driven hybrid interphase enabling stable versatile zinc metal electrodes for aqueous zinc batteries

Dingtao Ma[1]✉, Fan Li[1], Kefeng Ouyang[1], Qiuting Chen[1], Jinlai Zhao[2]✉, Minfeng Chen[3], Ming Yang[1], Yanyi Wang[1]✉, Jizhang Chen[3], Hongwei Mi[1,4], Chuanxin He[1,4] & Peixin Zhang[1,4]✉

[1] College of Chemistry and Environmental Engineering, Shenzhen University, 518060 Shenzhen, China

[2] College of Materials Science and Engineering, Shenzhen University, 518060 Shenzhen, China

[3] College of Materials Science and Engineering, Nanjing Forestry University, 210037 Nanjing, China

[4] Guangdong Flexible Wearable Energy and Tools Engineering Technology Research Center, 518060 Shenzhen, China

✉e-mail: mdt2500@szu.edu.cn; zhaojl@szu.edu.cn; wyy1984@szu.edu.cn; pxzhang@szu.edu.cn

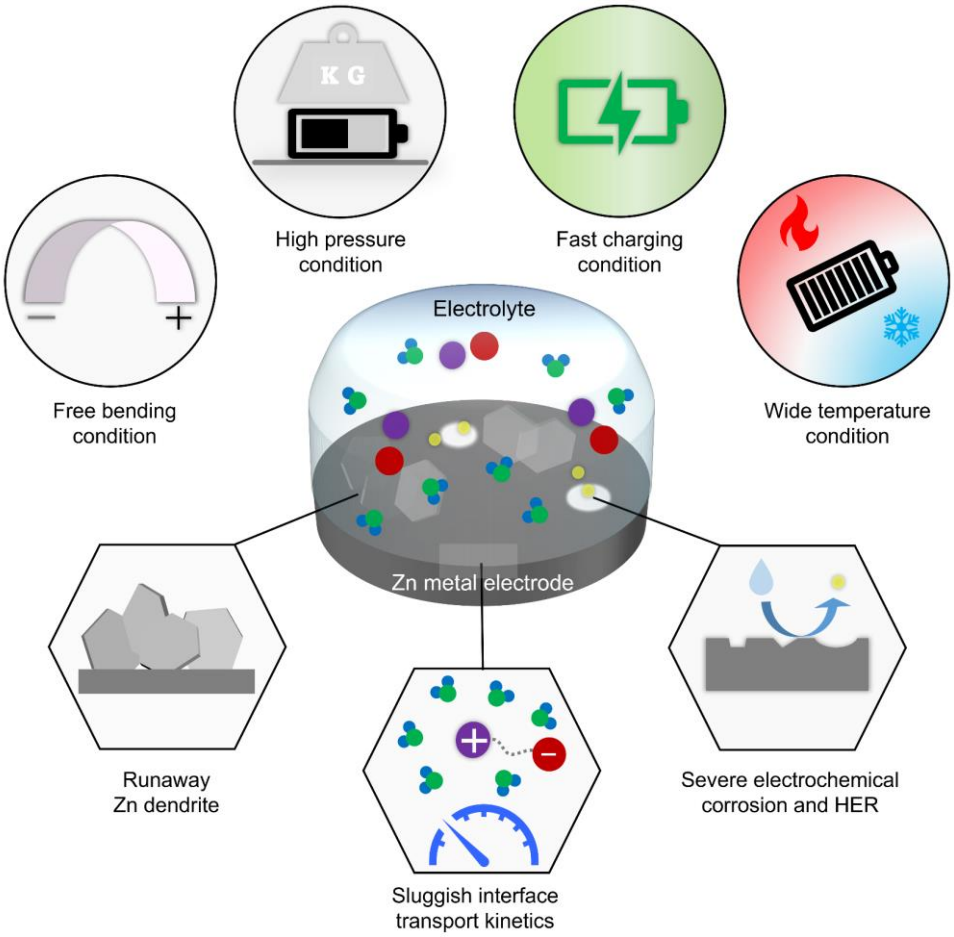

Supplementary Fig. 1 | Schematic diagram of stable versatile Zn metal electrode.

As depicted in Supplementary Fig. 1, the development of desirable Zn metal electrode should be adaptable to different application scenarios, thus enabling to support the practical requirements including fast-charging, wide-temperature, and bending-, pressure-tolerance conditions. Note that this figure was designed by using PowerPoint 2019 with permission proof.

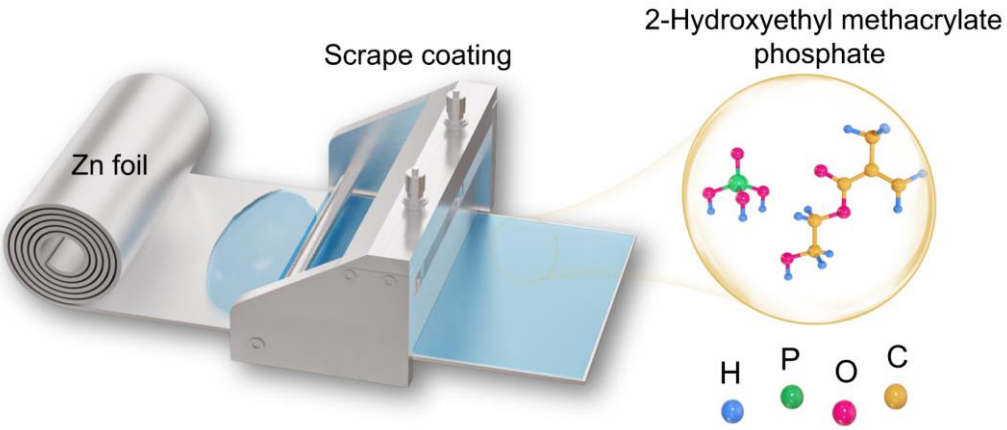

Supplementary Fig. 2 | Schematic diagram of the preparation process of SEI Zn.

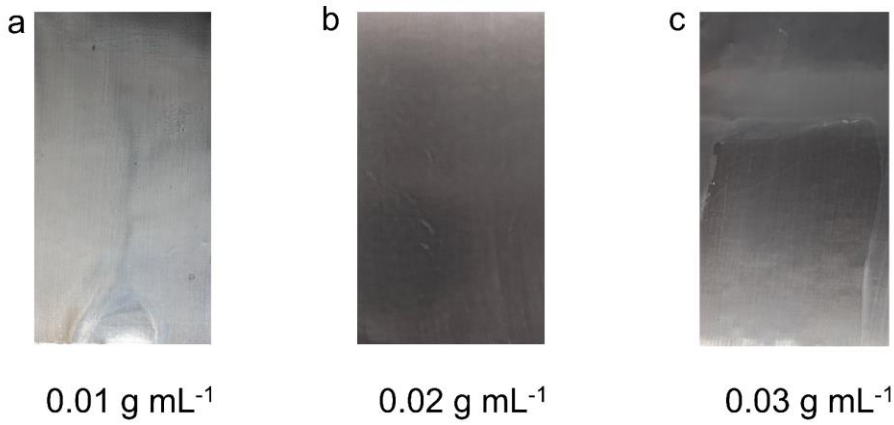

Supplementary Fig. 3 | Optical images of SEI Zn prepared by scraping coating with solutions of different MAHEPE concentrations. (a) 0.01 g mL^{-1}, (b) 0.02 g mL^{-1}, (c) 0.03 g mL^{-1}.

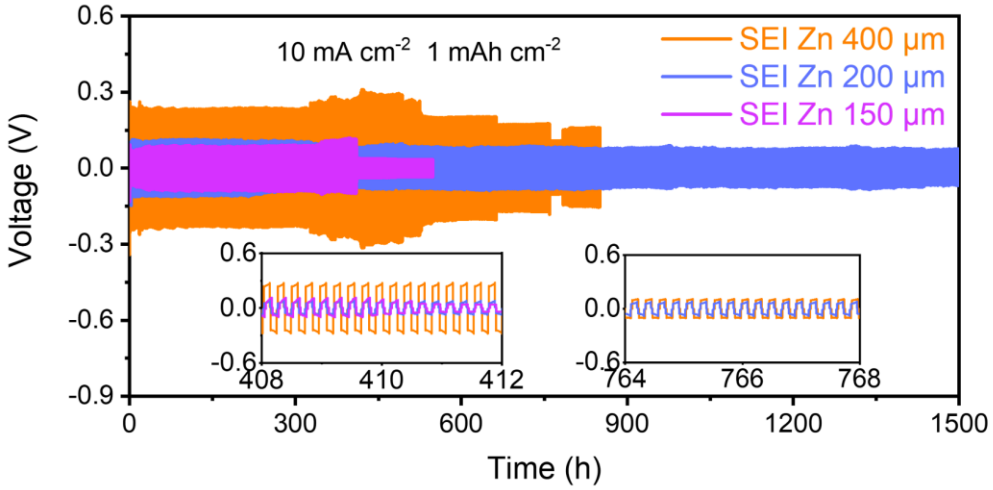

Supplementary Fig. 4 | Long cycle performance of Zn||Zn symmetric cells assembled with SEI Zn prepared by scraping coating with different thicknesses.

In initial investigation of the process conditions, the influence of the concentration of MAHEPE dispersed in ethanol was investigated. Specifically, solutions with concentrations of 0.01 g mL^{-1}, 0.02 g mL^{-1}, and 0.03 g mL^{-1} were prepared, while all other conditions were held constant. These solutions were subsequently applied to Zn foil via a scraping technique (Supplementary Fig. 3). Experimental outcomes revealed that solutions with concentrations of 0.01 g mL^{-1} and 0.03 g mL^{-1} resulted in non-uniform coatings. This phenomenon may be attributed to the insufficient viscosity of the thinner solution, preventing adequate adhesion of organic matter to the Zn metal surface, and the excessive concentration of the thicker solution, leading to uneven scraping. Consequently, a solution concentration of 0.02 g mL^{-1} was selected for further study.

Subsequently, we explored the optimal thickness of the scraped coating. Using the 0.02 g mL^{-1} solution, SEI Zn electrodes with thicknesses of 150 μm, 200 μm, and 400 μm were fabricated and assembled into Zn||Zn symmetric batteries. These batteries underwent long-cycle testing at a current density of 10 mA cm^{-2} with a capacity of 1 mAh cm^{-2} at 25°C (Supplementary Fig. 4). The results indicated that the electrode with a 400 μm thickness exhibited a larger polarization voltage, whereas the electrode with

a 150 μm thickness short-circuited within 420 h. Notably, the 200 μm SEI Zn||Zn symmetric battery demonstrated stable cycling for 1500 h, demonstrating excellent reversibility of Zn deposition/stripping. Therefore, 200 μm was selected as the best scraping thickness in this research.

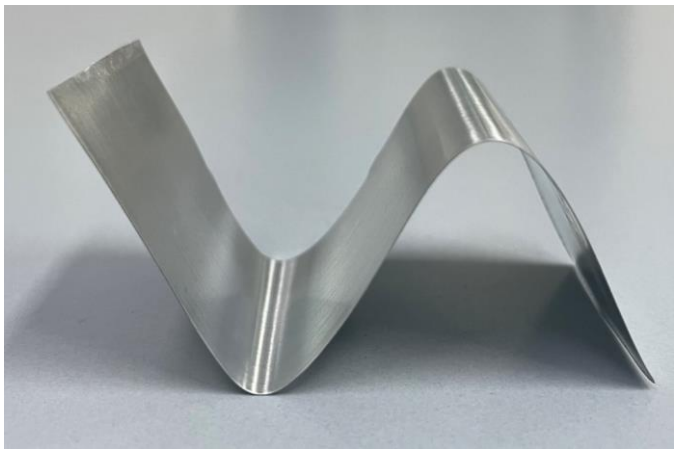

Supplementary Fig. 5 | Digital image of SEI Zn at the bending state.

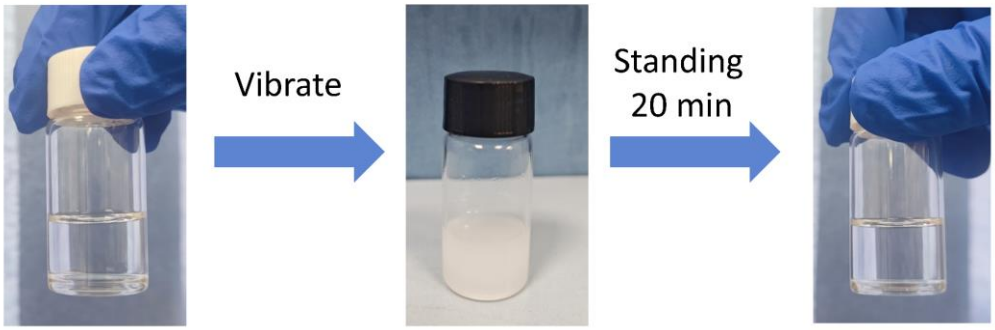

Supplementary Fig. 6 | Water solubility test of MAHEPE.

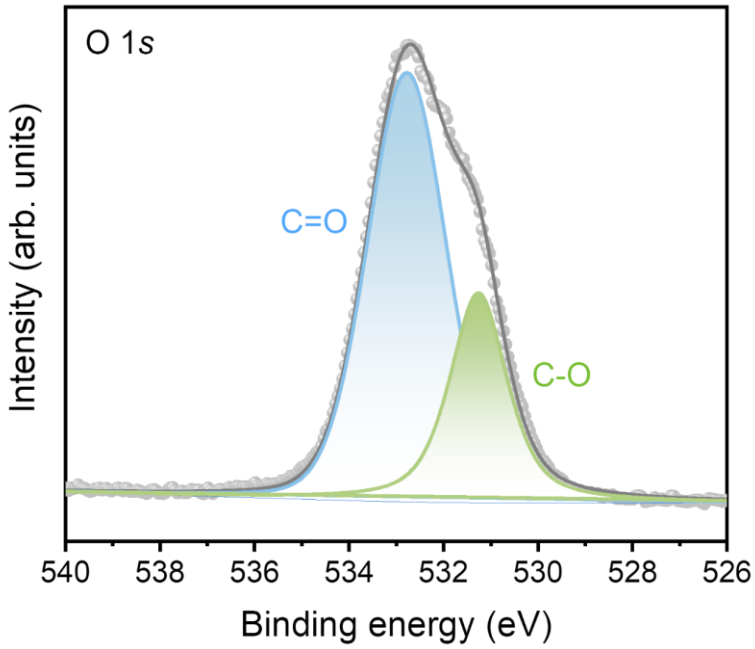

Supplementary Fig. 7 | O 1*s* XPS spectra of SEI Zn.

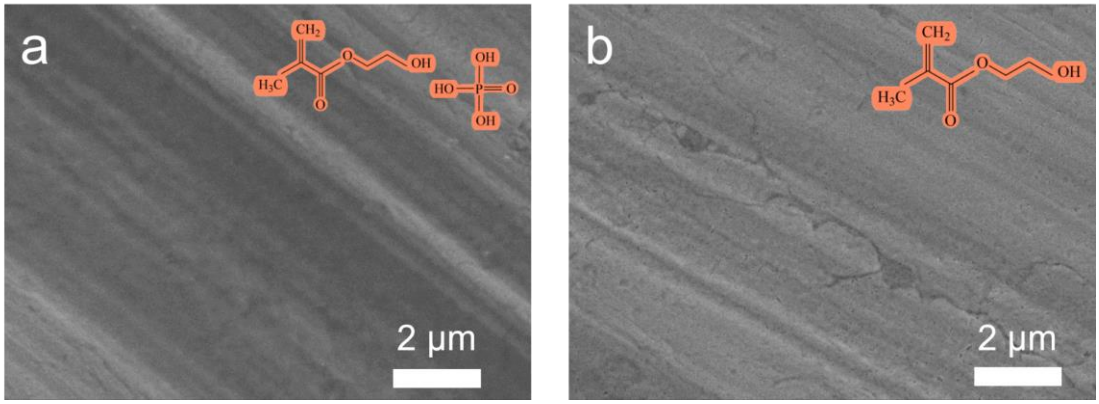

Supplementary Fig. 8 | FESEM images of (a) SEI Zn and (b) 2-methyl-2-hydroxyethyl acrylate coated Zn foil soaked in 3 M $ZnSO_4$ electrolyte for 12 h.

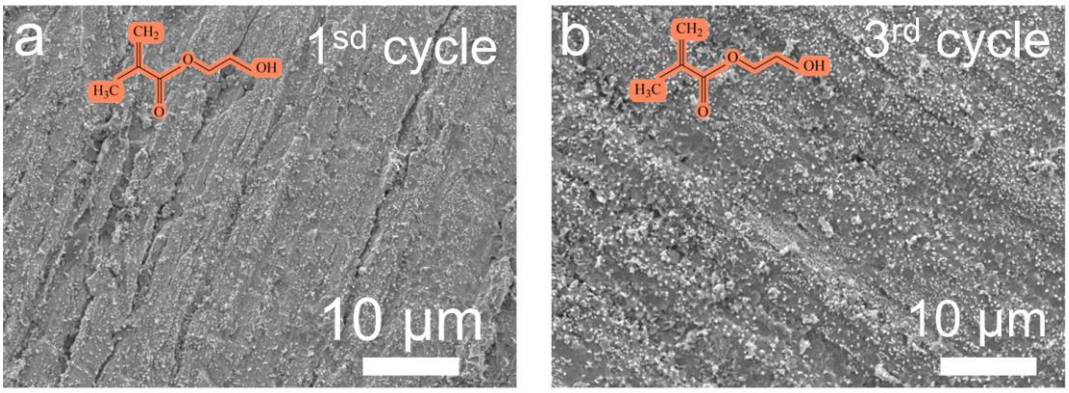

Supplementary Fig. 9 | FESEM images of the 2-methyl-2-hydroxyethyl acrylate coated Zn foil (a) after 1 cycle and (b) after 3 cycles.

To investigate the composition and formation mechanism of these dots, we conducted comparative experiments. To determine whether the formation of these visible dots is related to phosphate groups in the SEI, we used 2-methyl-2-hydroxyethyl acrylate, which has a molecular structure highly similar to that of 2-methyl-2-acrylate-2-hydroxyethyl ester phosphate ester but without phosphate groups, as a coating material to prepare Zn anodes. As shown in Supplementary Fig. 8, after immersion in 3 M $ZnSO_4$ for 12 h, no visible dot structures were observed on the surface of the SEI Zn and 2-methyl-2-hydroxyethyl acrylate coated Zn, indicating that the formation of these dots is unlikely to be a non-electrochemical process. However, after Zn deposition/stripping on the 2-methyl-2-hydroxyethyl acrylate coated Zn, uniformly distributed dots gradually appeared on the surface (Supplementary Fig. 9). It can be defined that this dot-like structure is likely derived from electrochemical decomposition of organic components.

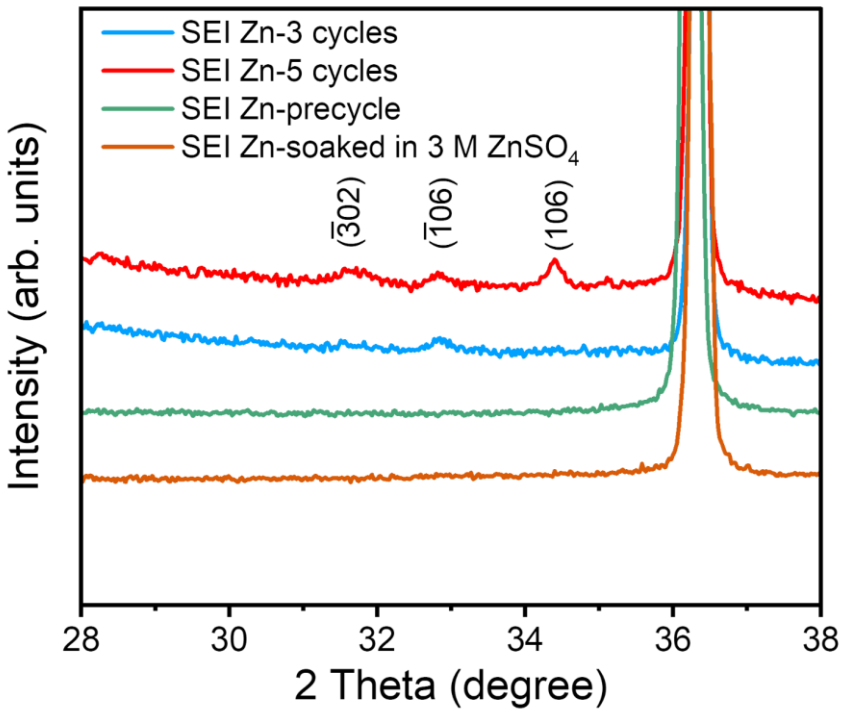

Supplementary Fig. 10 | XRD patterns of the cycled SEI Zn, precycle SEI Zn and soaked SEI Zn surface.

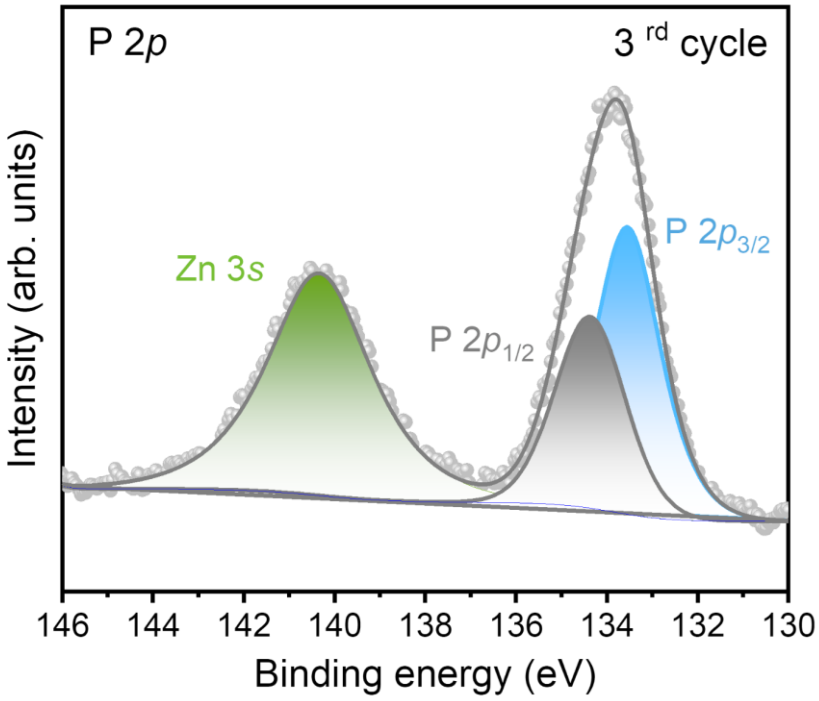

Supplementary Fig. 11 | P 2*p* XPS spectra of SEI Zn surface after 3 cycles.

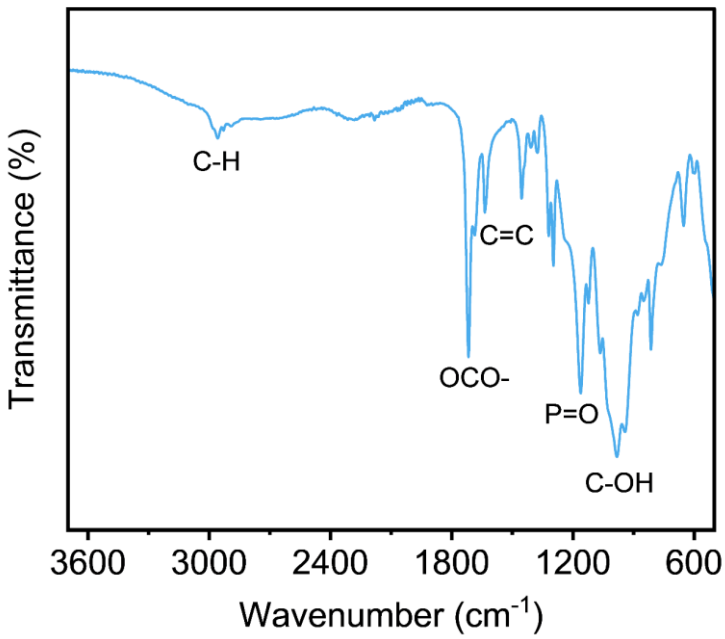

Supplementary Fig. 12 | FTIR spectra of SEI Zn surface after 3 cycles.

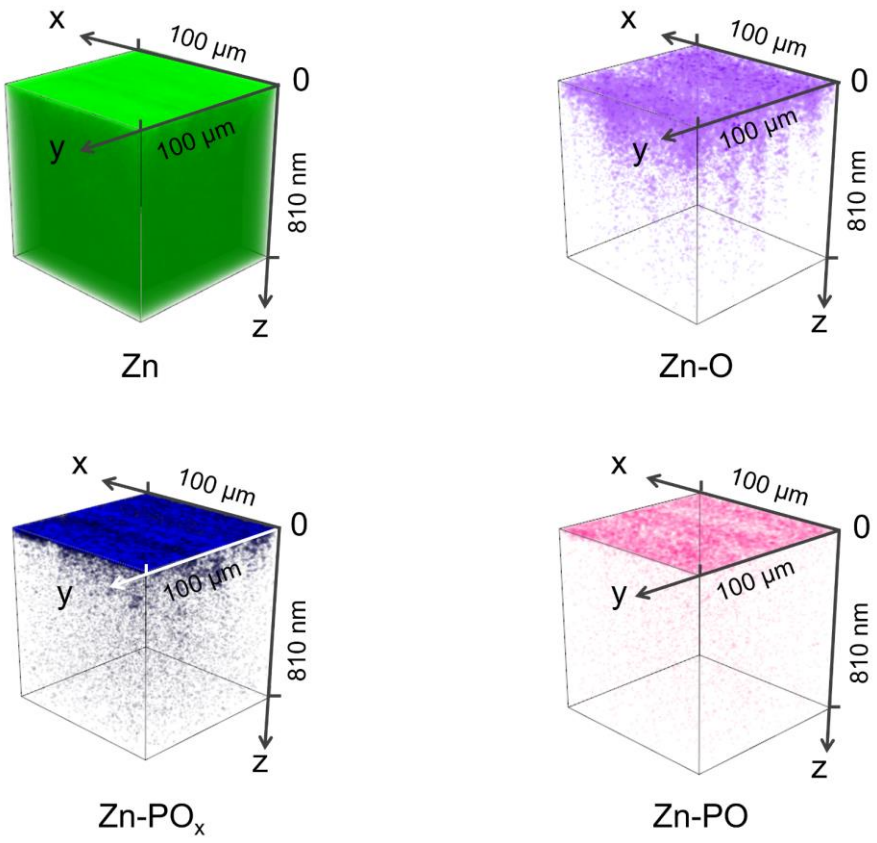

Supplementary Fig. 13 | TOF-SIMS 3D reconstruction of SEI Zn surface before cycling (Positive ion mode was selected. Note that the scales of the x-axis and y-axis are different from those of the z-axis direction. The former represents the raster size and the latter means the sputter depth. Among them, the raster size is 100 μm×100 μm, the sputter rate is 0.45 nm s^{-1} on SiO_2 with a sputter time of 1800 s).

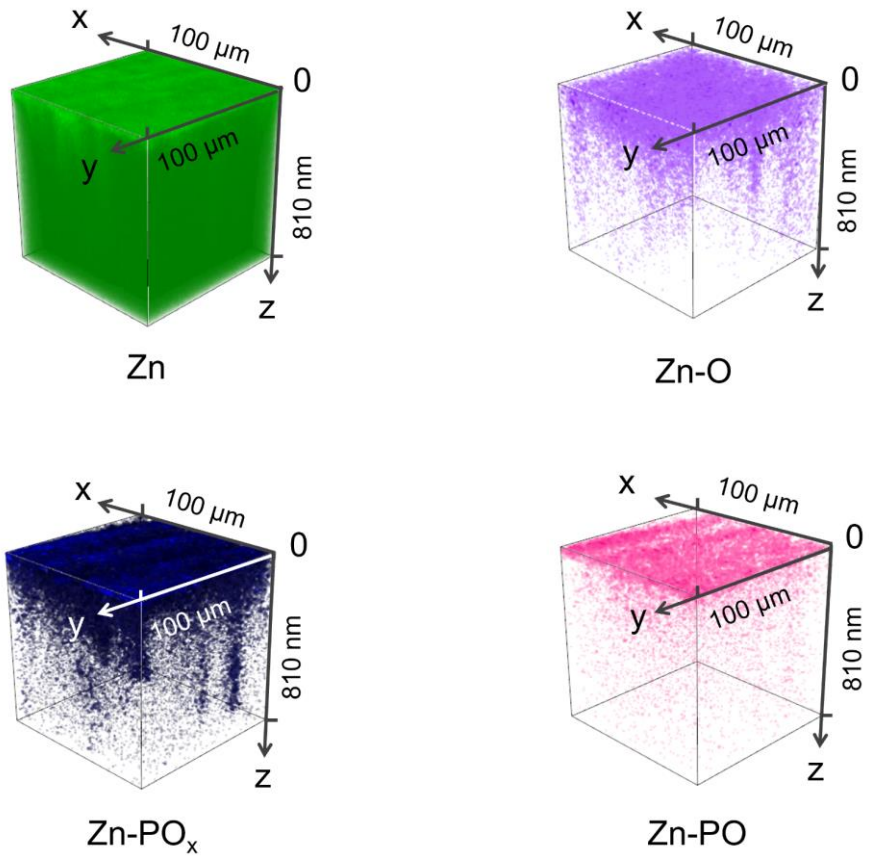

Supplementary Fig. 14 | TOF-SIMS 3D reconstruction of SEI Zn surface after 3 cycles (Positive ion mode was selected. Note that the scales of the x-axis and y-axis are different from those of the z-axis direction. The former represents the raster size and the latter means the sputter depth. Among them, the raster size is 100 μm×100 μm, the sputter rate is 0.45 nm s^{-1} on SiO_2 with a sputter time of 1800 s).

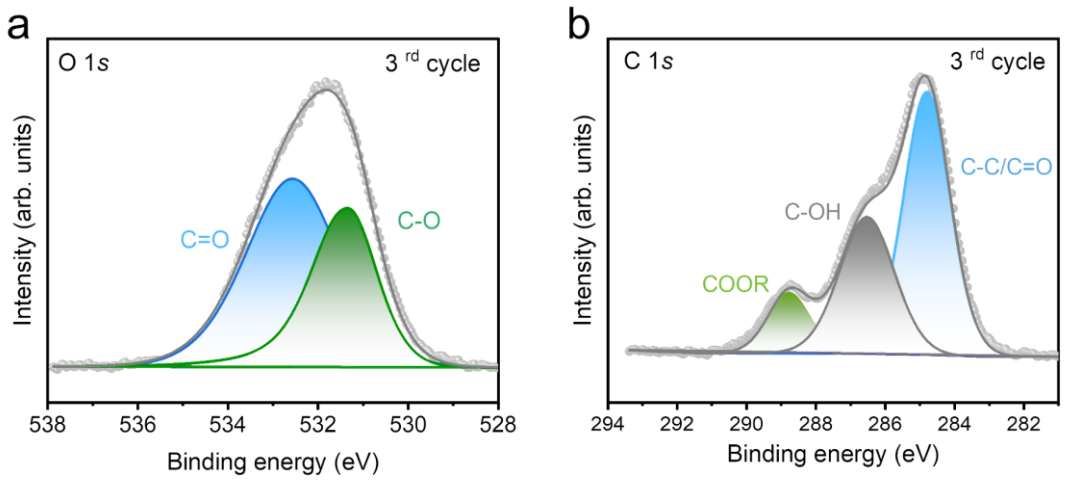

Supplementary Fig. 15 | Chemical composition and elemental state analysis of the SEI Zn electrode after 3 cycles. (a) O 1*s* and (b) C 1*s* XPS spectra of SEI Zn.

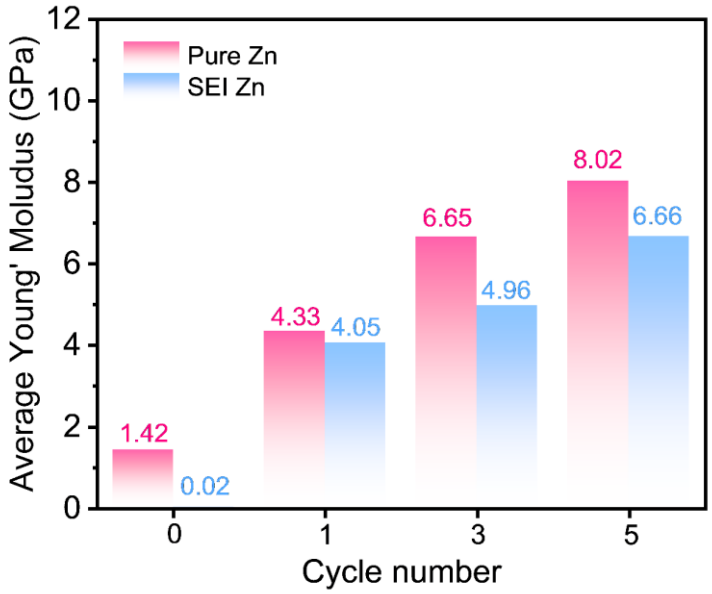

Supplementary Fig. 16 | The AYM columnar statistics of Pure Zn and SEI Zn electrodes.

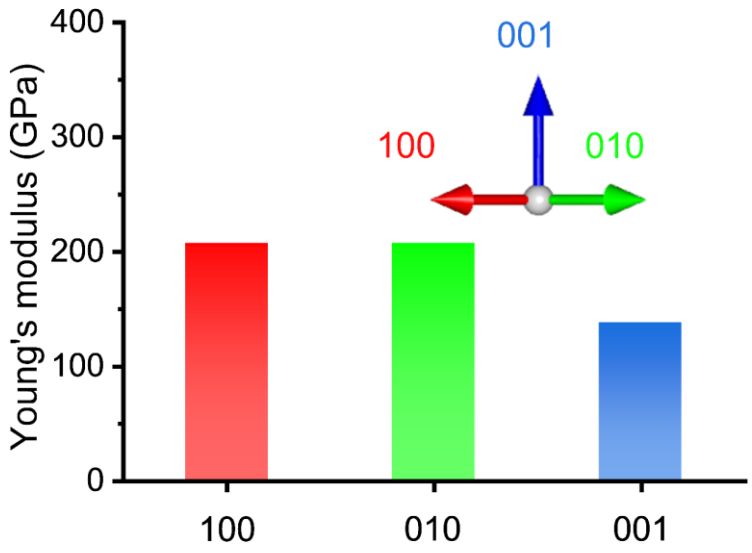

Supplementary Fig. 17 | The Young's modulus of Zn along different crystal axes, and a schematic diagram of the crystal axis directions.

The higher average AYM of Zn dendrites can be attributed to the dominant orientation of crystal planes in the vertical growth direction. Here, the theoretical research of Young's modulus was carried out by the following Methodology.

All the calculations are implemented by the VASP code. The GGA-PBE functional is selected for the exchange and correlation potential. Weak van der Waals interaction is considered by the DFT-D3 functional. The cut off energy for the plane-wave is 400 eV. The Gamma point in the Brillouin-zone is chosen for integration. Total energies of the systems converge to 10^{-5} eV in the iteration solution of Kohn-Sham equation. The force on each atom reduce to 0.05 eV/Å after geometry optimization. Then, the elastic constants are determined using second-order derivatives of equilibrium energy with respect to strains via the following equation:

$$C_{\alpha\beta} = \frac{1}{V}\frac{\partial^2 E}{\partial\gamma\alpha\partial\gamma\beta}$$

where γ's are applied strains in Voigt's notion around the equilibrium position. The average Young's modules and the directional dependence are derived from the elastic constants.

Specifically, the Young's modulus varies with the crystallographic axes, with the Zn [100] and Zn [010] axes (representing vertical directions) exhibiting a higher modulus of 207 GPa, compared to the Zn [001] axis (representing the horizontal direction) with a lower modulus of 137.417 GPa. In vertically growing dendrites, the crystal planes oriented along the high-modulus axes (Zn [100] and Zn [010]) are predominant. As a result, the measured Young's moduli along these axes are higher, leading to an elevated AYM for the dendrites compared to pure Zn.

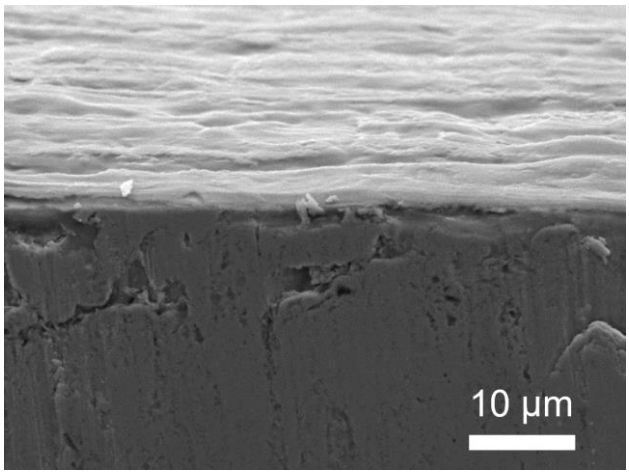

Supplementary Fig. 18 | Side-view FESEM image of SEI Zn after 5 cycles.

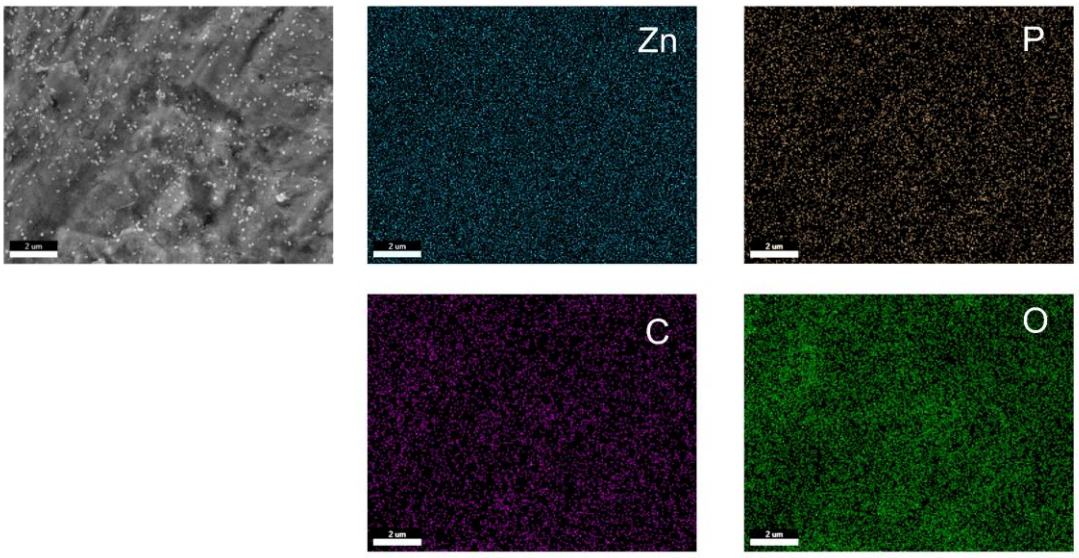

Supplementary Fig. 19 | EDS mapping image of SEI Zn after 5 cycles.

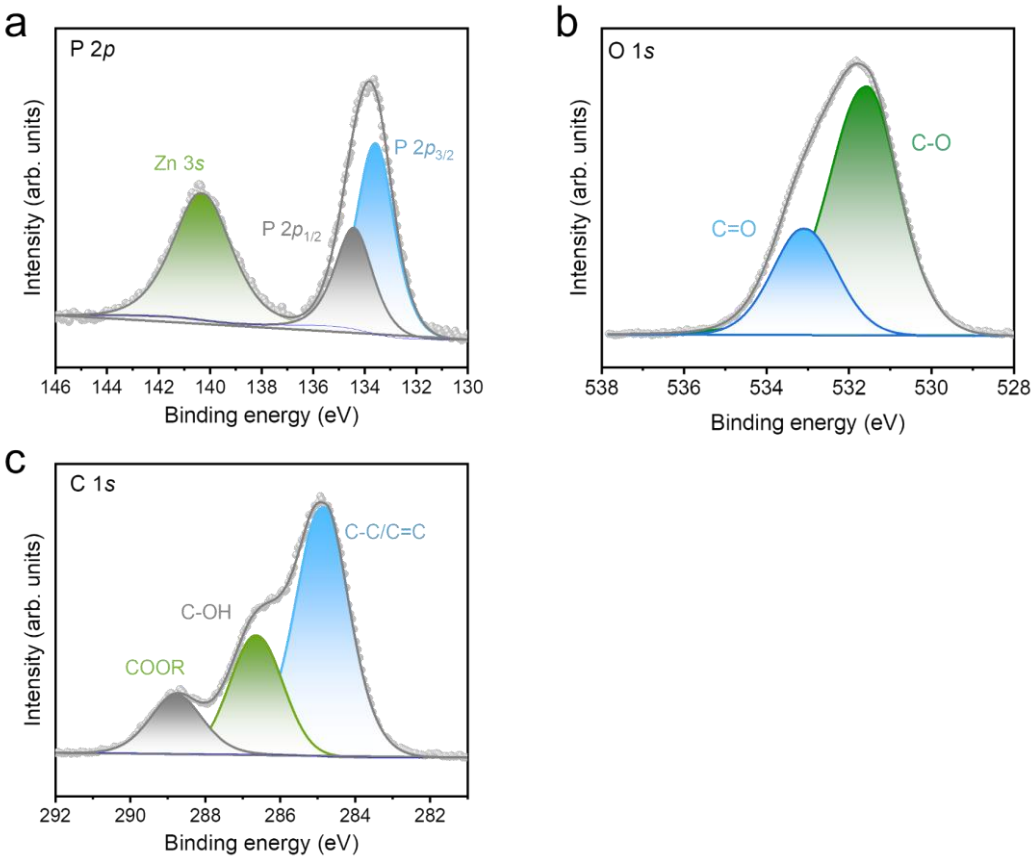

Supplementary Fig. 20 | Chemical composition and elemental state analysis of SEI Zn electrode after 5 cycles. (a) P 2*p*, (b) O 1*s* and (c) C 1*s* XPS spectra of SEI Zn.

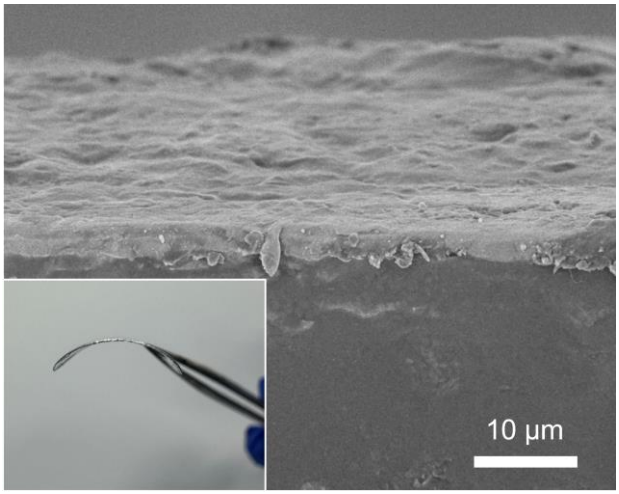

Supplementary Fig. 21 | Side view FESEM image of SEI Zn anode after 20 cycles at the bending state.

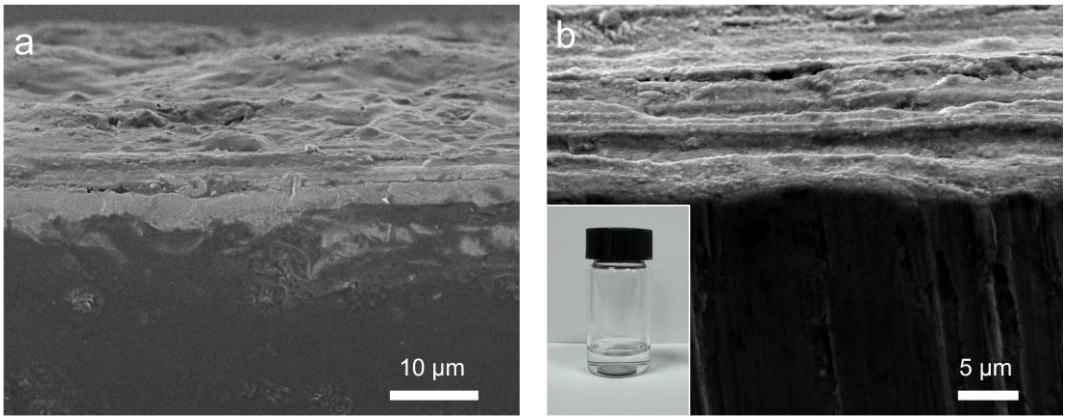

Supplementary Fig. 22 | Side view FESEM images of SEI Zn electrodes after 50 cycles, (a) without and (b) with electrolyte soaking treatment for 30 min.

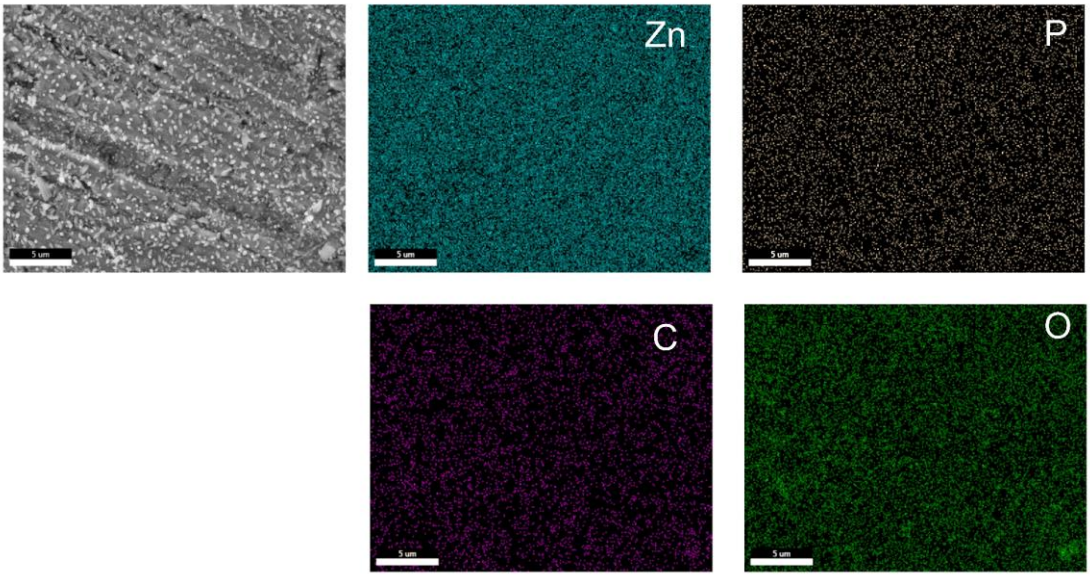

Supplementary Fig. 23 | EDS mapping image of SEI Zn after 10 cycles.

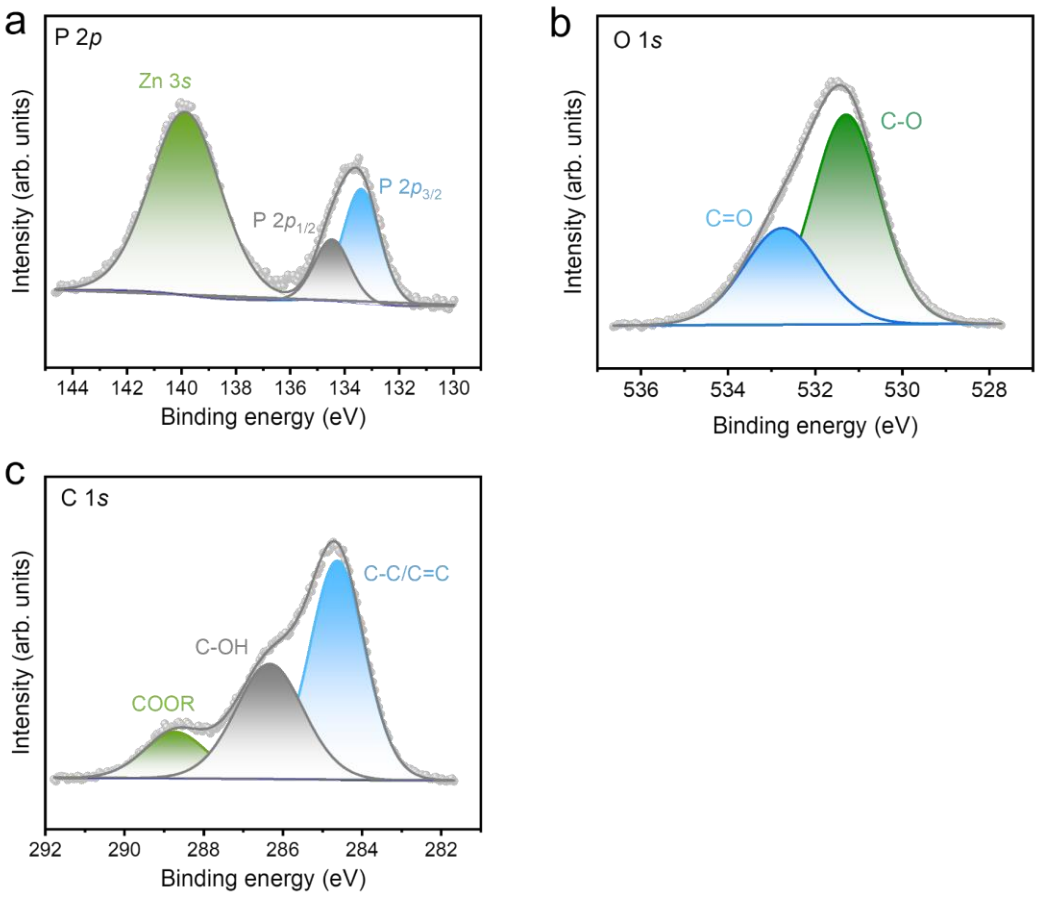

Supplementary Fig. 24 | Chemical composition and elemental state analysis of SEI Zn electrode after 10 cycles. (a) P 2*p* (b) O 1*s* and (c) C 1*s* XPS spectra of SEI Zn.

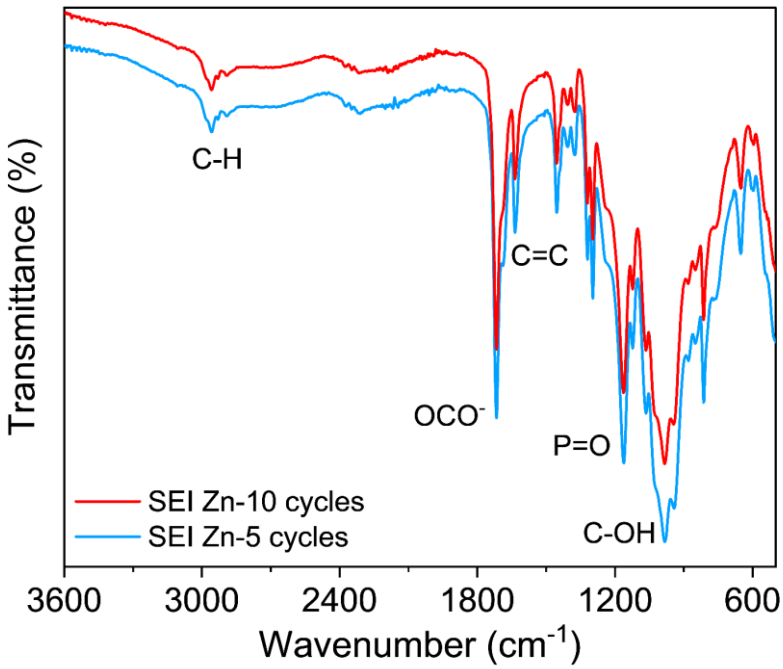

Supplementary Fig. 25 | FTIR Spectra of SEI Zn electrode after 5 and 10 cycles.

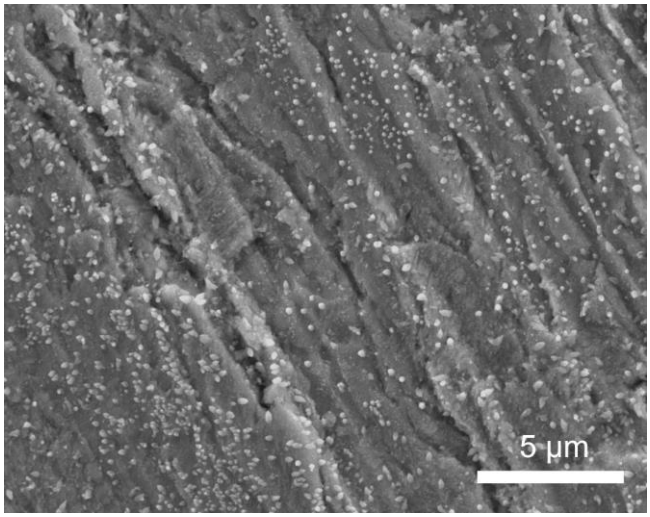

Supplementary Fig. 26 | FESEM images of SEI Zn electrode after 100 cycles.

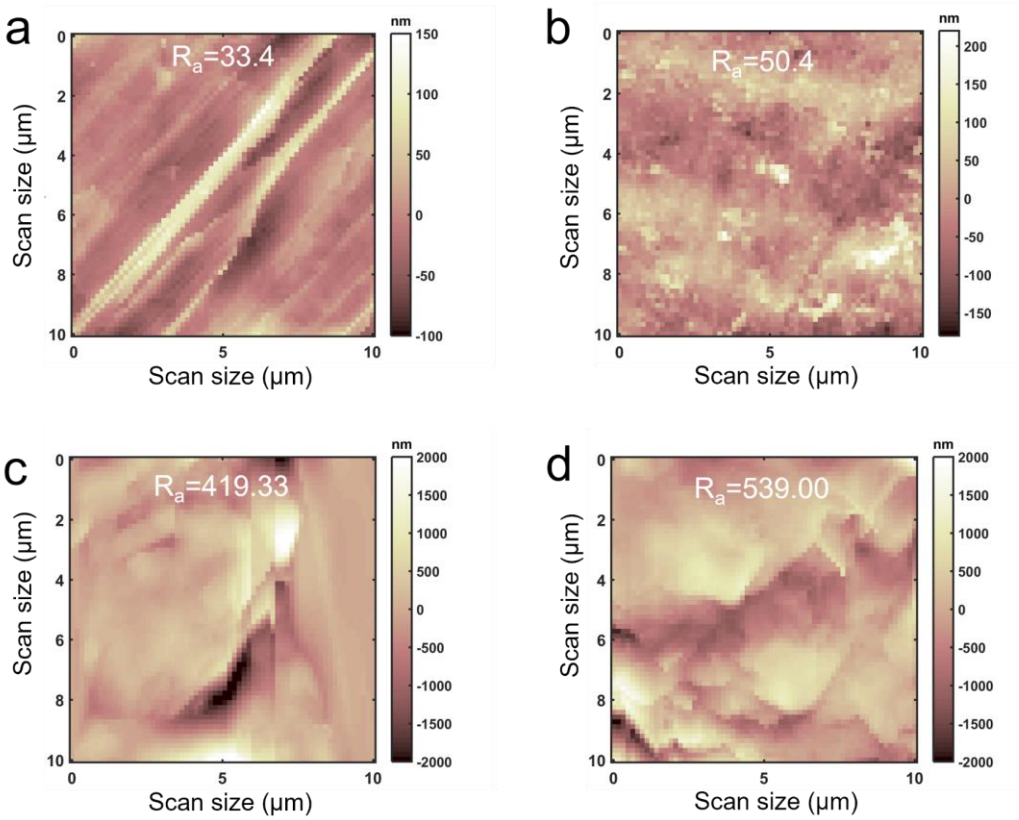

Supplementary Fig. 27 | Research on the morphological evolution of pure Zn electrode. The AFM morphology of Pure Zn electrode (a) before cycle, after (b) 1st cycle, (c) 3rd cycle, and (d) 5th cycle.

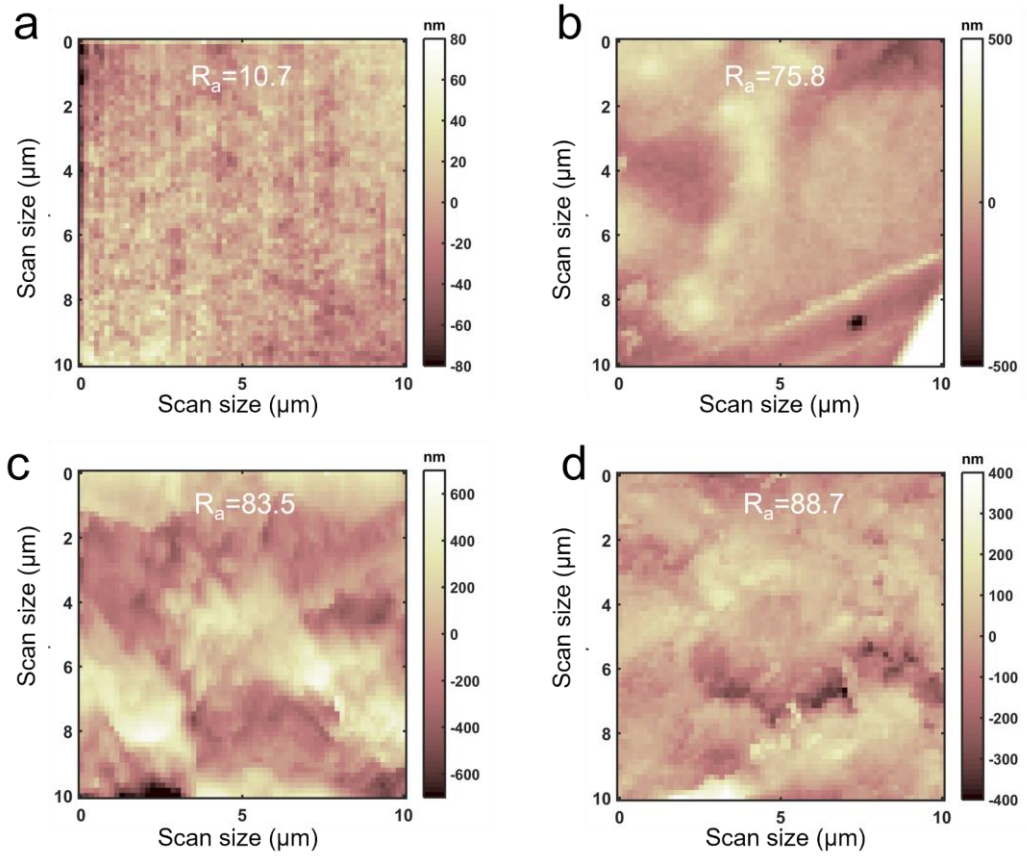

Supplementary Fig. 28 | Research on the morphological evolution of SEI Zn electrode. The AFM morphology of SEI Zn electrode (a)before cycle, after (b) 1st cycle, (c) 3rd cycle, and (d) 5th cycle.

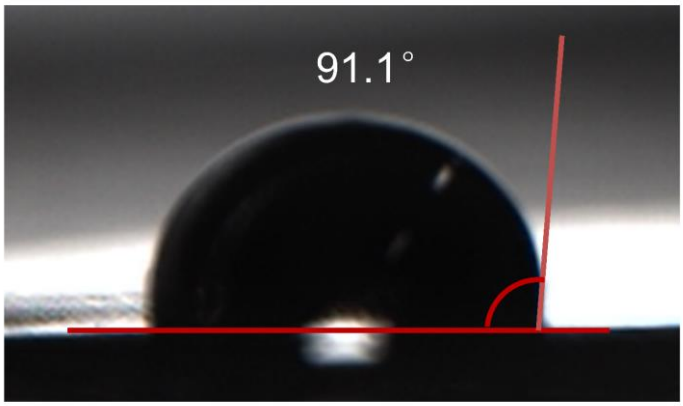

Supplementary Fig. 29 | Contact angle test on the surface of the cycled SEI Zn by using 3 M $ZnSO_4$ aqueous electrolyte.

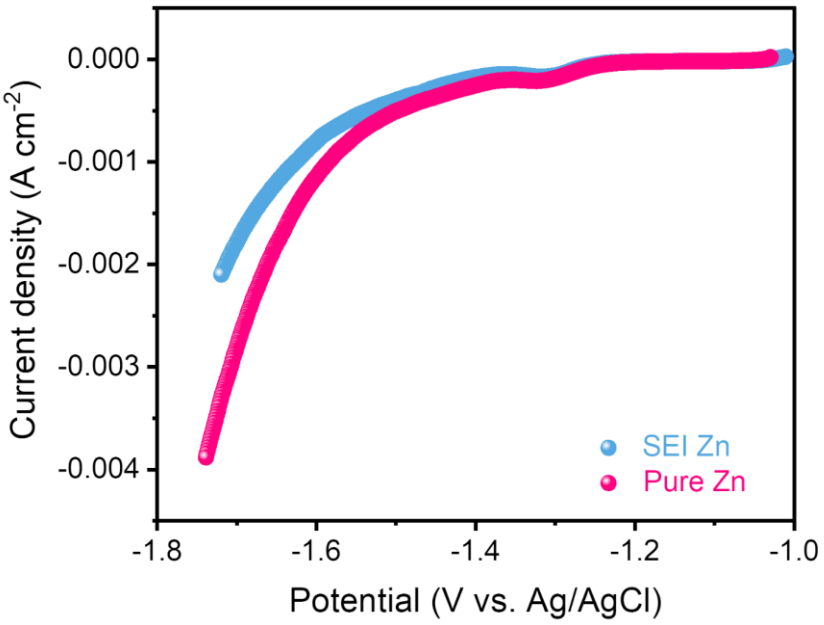

Supplementary Fig. 30 | LSV curves of the Pure Zn and SEI Zn electrodes tested in 1 M Na_2SO_4 electrolyte.

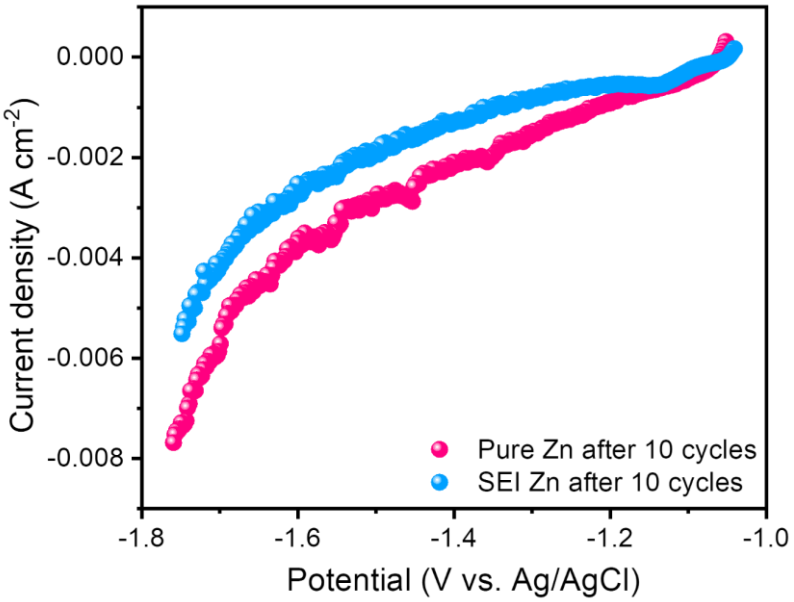

Supplementary Fig. 31 | LSV curves of the Pure Zn and SEI Zn electrodes after 10 cycles tested in 1 M Na_2SO_4 electrolyte.

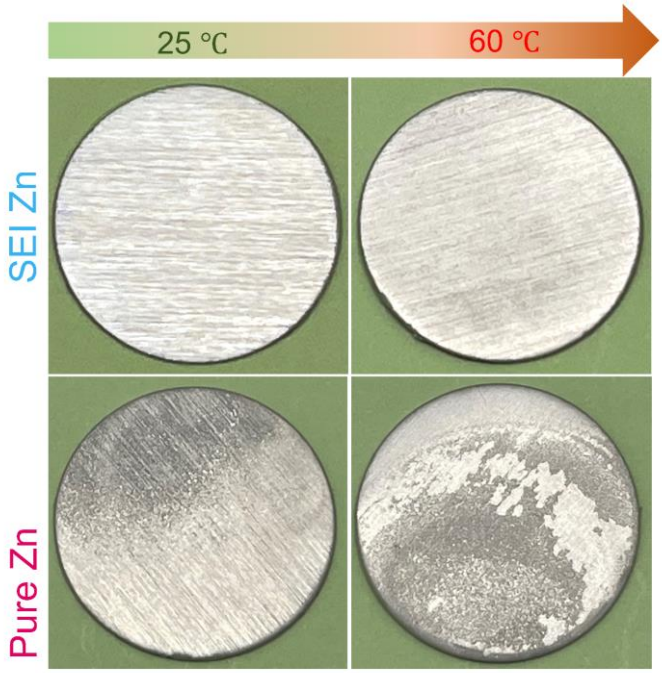

Supplementary Fig. 32 | Digital photos of Pure Zn and SEI Zn electrodes soaked in $ZnSO_4$ electrolyte at different temperatures.

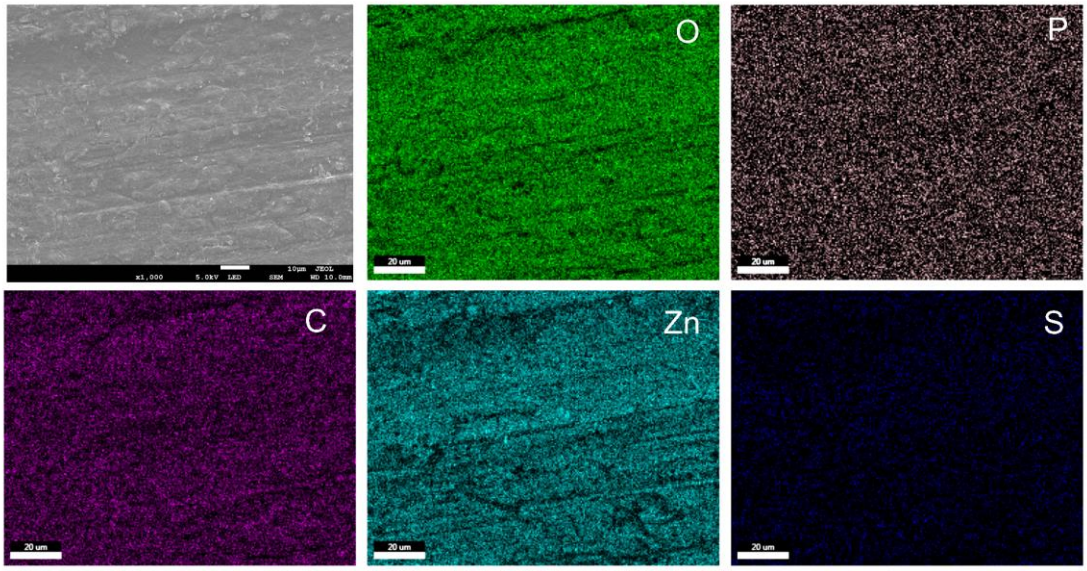

Supplementary Fig. 33 | FESEM and corresponding EDS spectra of the SEI Zn electrode soaked in $ZnSO_4$ electrolyte at room temperature.

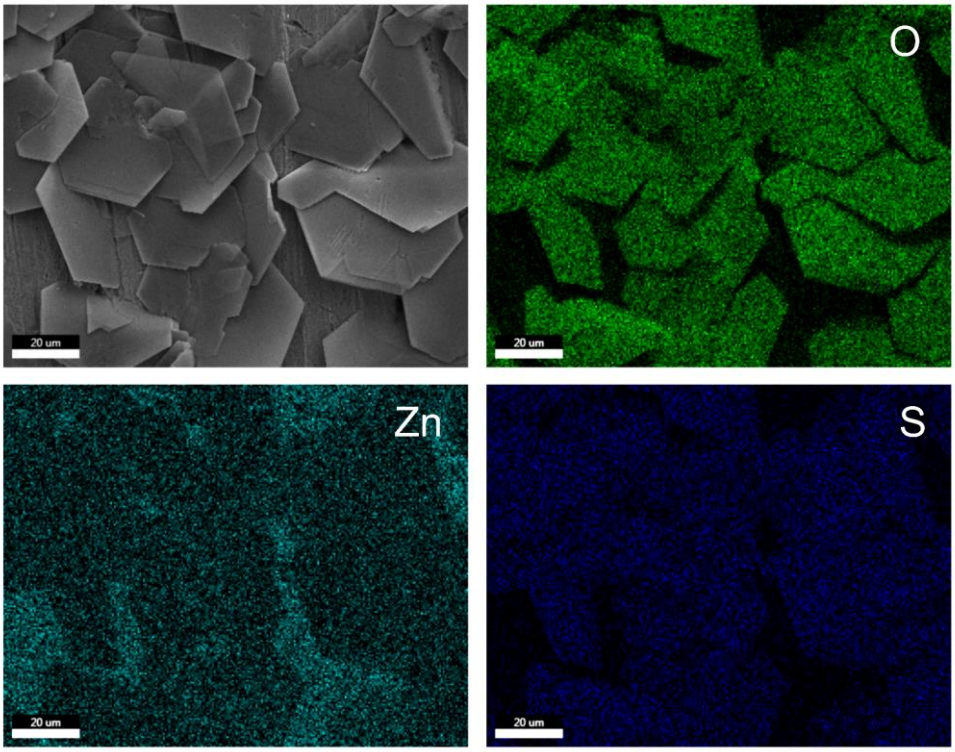

Supplementary Fig. 34 | FESEM and corresponding EDS spectra of the Pure Zn electrode soaked in $ZnSO_4$ electrolyte at room temperature.

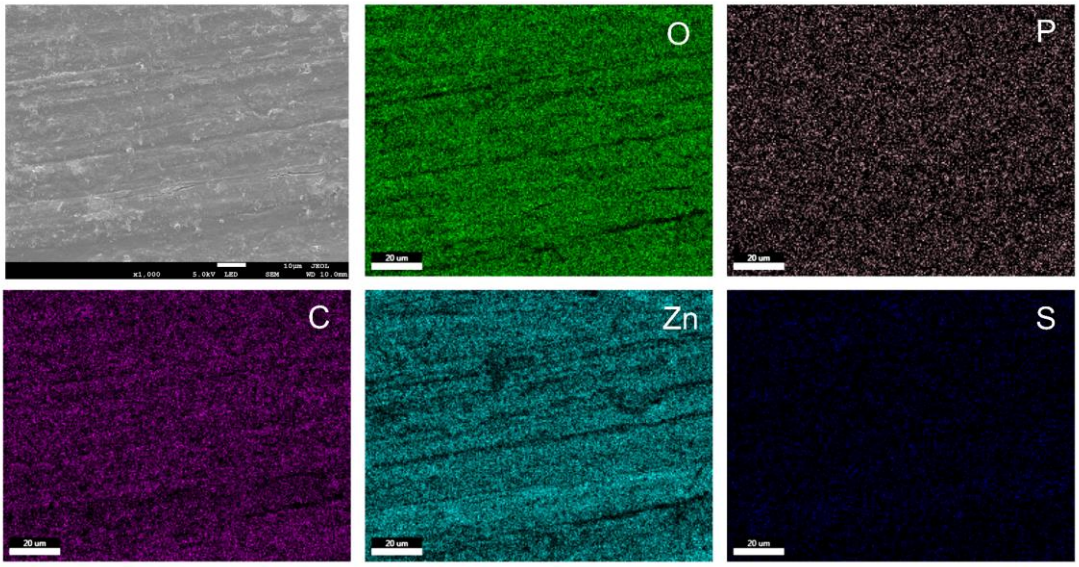

Supplementary Fig. 35 | FESEM and corresponding EDS spectra of the SEI Zn electrode soaked in $ZnSO_4$ electrolyte at 60℃.

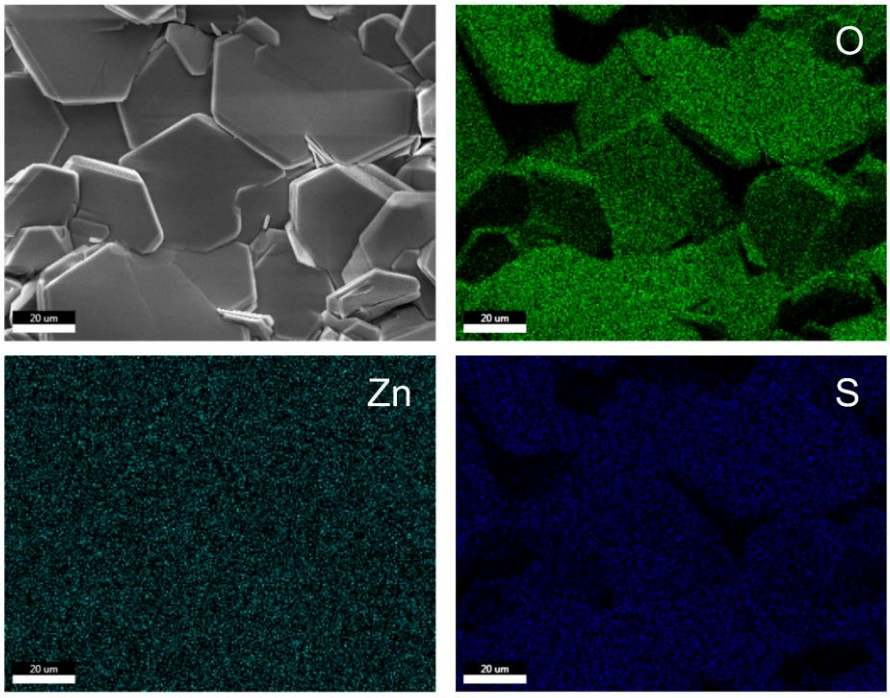

Supplementary Fig. 36 | FESEM and corresponding EDS spectra of the Pure Zn electrode soaked in $ZnSO_4$ electrolyte at 60℃.

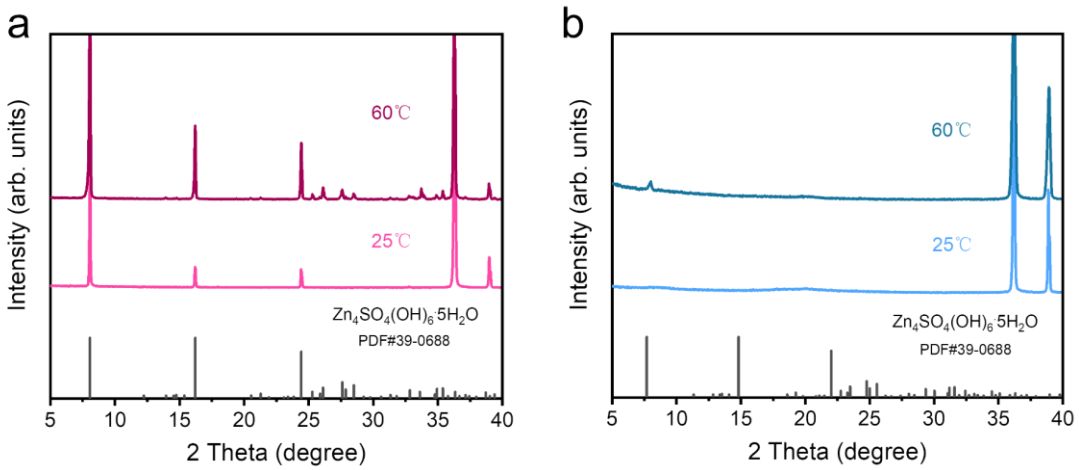

Supplementary Fig. 37 | The XRD patterns of (a) Pure Zn and (b) SEI Zn electrodes after soaking at different temperature.

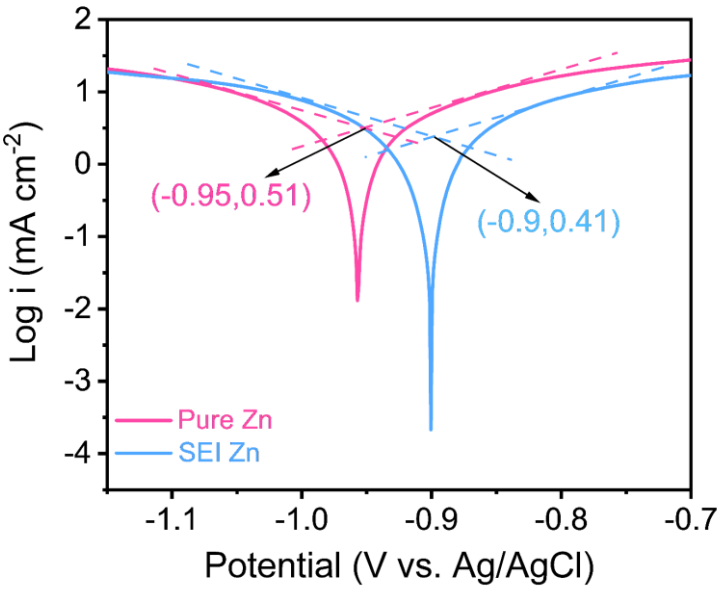

Supplementary Fig. 38 | Tafel curves of pure Zn and SEI Zn electrodes.

The Tafel test uses 3 M $ZnSO_4$ as the electrolyte, pure Zn or SEI Zn electrode as the working electrode, Pt electrode as the opposite electrode, and Ag/AgCl as the reference electrode. The test voltage range is -0.3 to 0.3 V (vs. OCP), and the sweep speed is 1 mV s^{-1}. The corrosion potential and corrosion current density is calculated by the following method, using the Tafel extrapolation method, the anode and cathode sections of the polarization curve were linearly fitted. With software such as Origin, the logarithm of the current density (log I) was plotted on the Y-axis and the potential (E) on the X-axis. By solving for the intersection point of the fitting lines, the corrosion potential (E_{corr}) was obtained. Subsequently, the corrosion potential was substituted into the fitting function to derive the corrosion current density (I_{corr}).

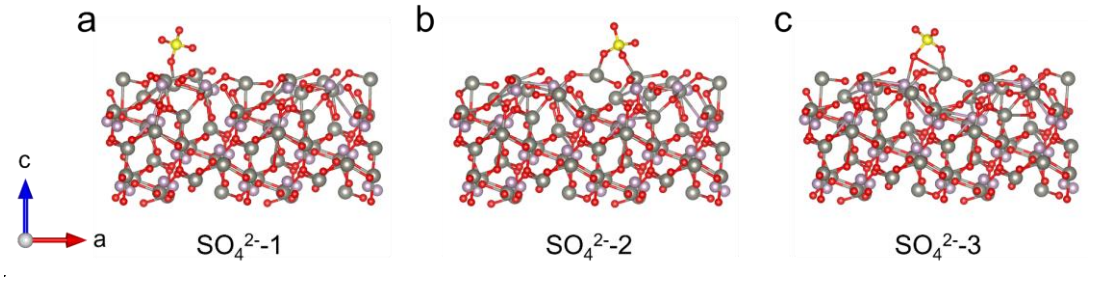

Supplementary Fig. 39 | Side view of different optimized structure models for SO_4^{2-} adsorption on $Zn_3(PO_4)_2$ surface: (a) SO_4^{2-}-1, (b) SO_4^{2-}-2 and (c) SO_4^{2-}-3.

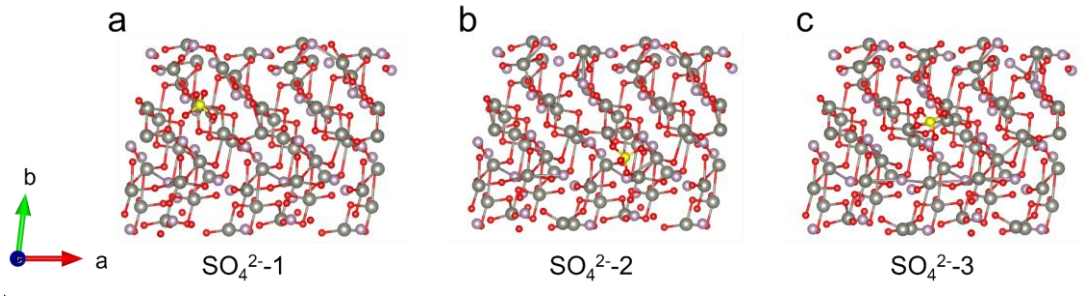

Supplementary Fig. 40 | Top view of different optimized structure models for SO_4^{2-} adsorption on $Zn_3(PO_4)_2$ surface: (a) SO_4^{2-}-1, (b) SO_4^{2-}-2 and (c) SO_4^{2-}-3.

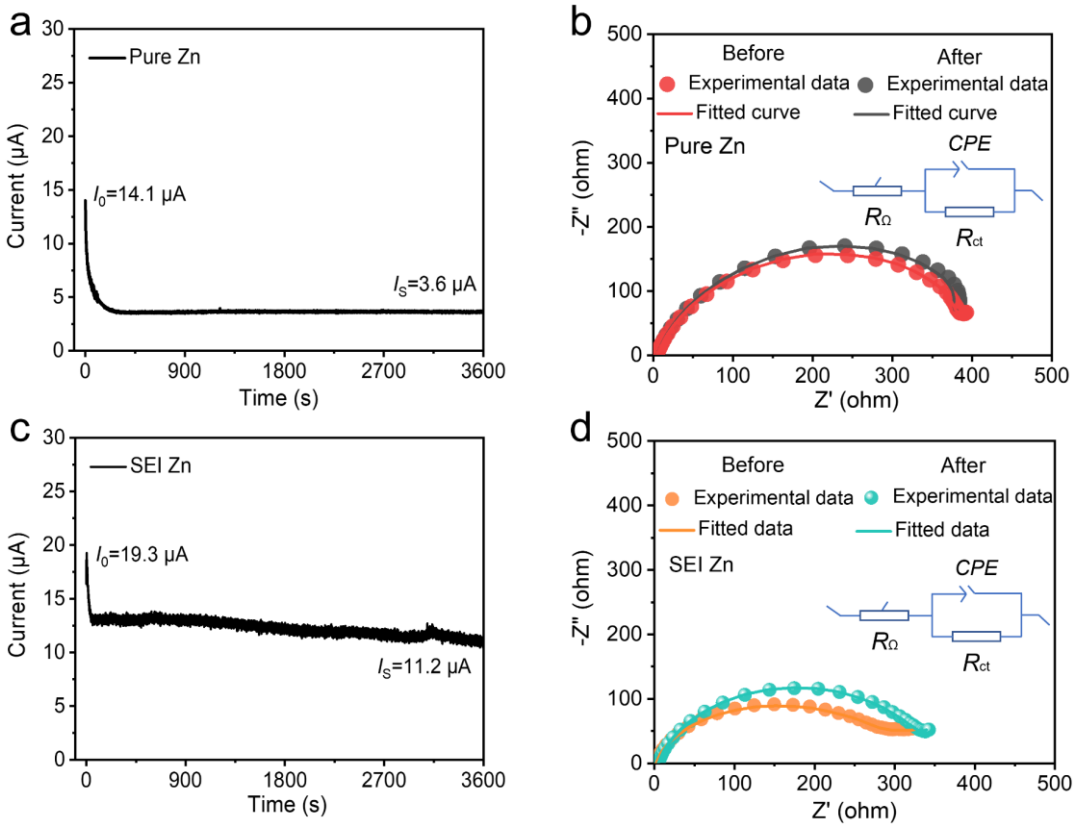

Supplementary Fig. 41 | Calculation of the Zn^{2+} transference number of Zn electrodes. Current-time curves of (a, b) Pure Zn and (c, d) SEI Zn, with a constant voltage polarization of 10 mV, and the impedance spectra before and after polarization (Note that their fitted results were displayed in **Supplementary Table 1**).

The transference number of Zn^{2+} (tz_n^{2+}) was tested in Zn||Zn symmetrical cells by EIS before and after the chronoamperometry (CA) tests and calculated by the following equation:

$$tz_n^{2+} = \frac{I_s(\Delta v - I_0 R_0)}{I_0(\Delta v - I_s R_s)}$$

where Δv is the applied voltage polarization. Here, the applied voltage polarization is 10 mV. I_s and R_s are the steady state current and resistance, respectively, and I_0 and R_0 are the initial current and resistance, respectively.

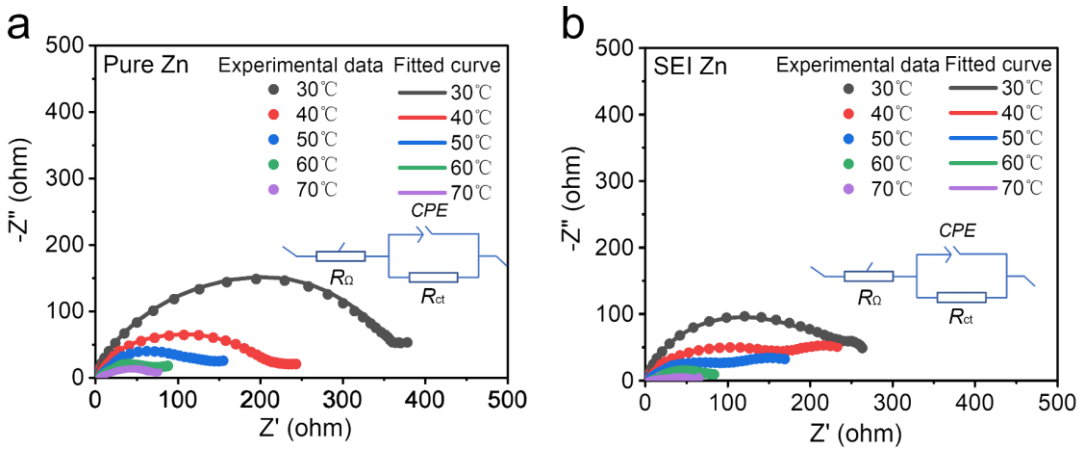

Supplementary Fig. 42 | Calculation of the activation energy of Zn electrodes. Impedance of symmetric batteries assembled with (a) Pure Zn and (b) SEI Zn at different temperatures (Note that their fitted results were displayed in **Supplementary Table 2)**.

According to the equation, the corresponding activation energy can be calculated.

$$ln(R_{ct}^{-1}) = ln\,A - E_a\,/\,RT$$

Where R_{ct} is the interfacial Zn^{2+} transfer resistance, E_a is the activation energy, T is the absolute temperature, R is the gas constant, and A is the pre-exponential factor.

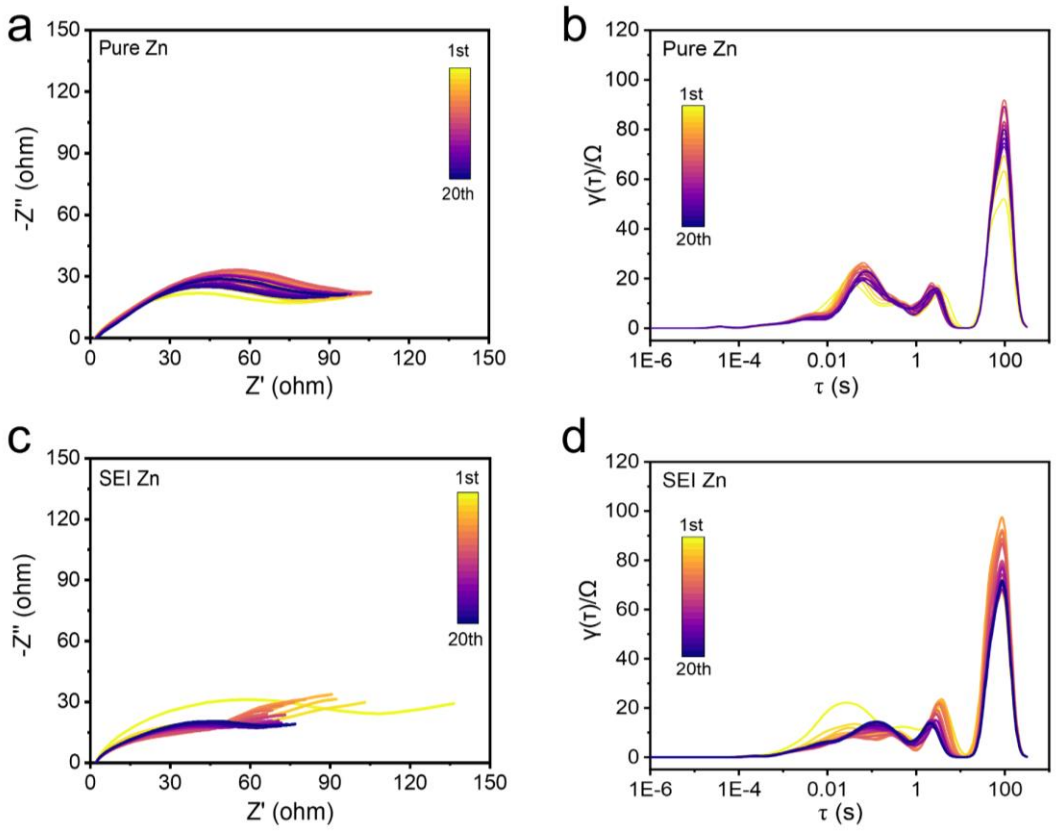

Supplementary Fig. 43 | Research on the electrochemical transport behavior of Zn electrodes. The Nyquist plots and DRT curves of the impedance spectra monitored for (a, b) Pure Zn and (c, d) SEI Zn electrodes.

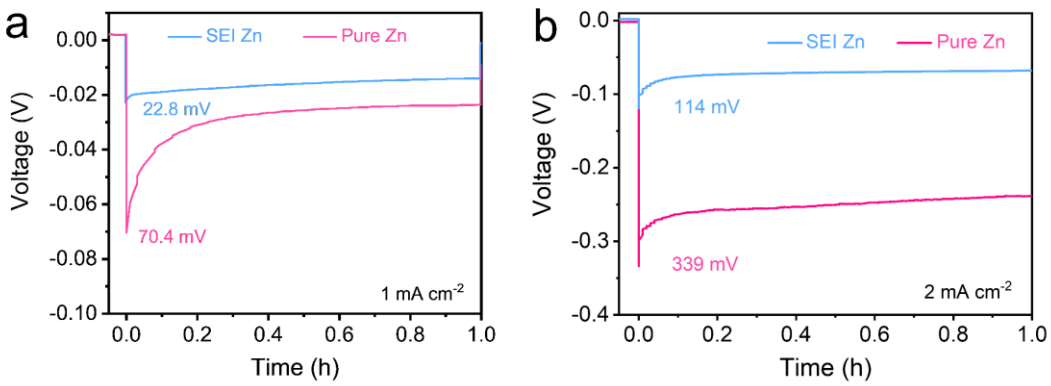

Supplementary Fig. 44 | Nucleation overpotential of Pure Zn and SEI Zn electrodes under the current densities of (a) 1 mA cm^{-2} and (b) 2 mA cm^{-2}, respectively.

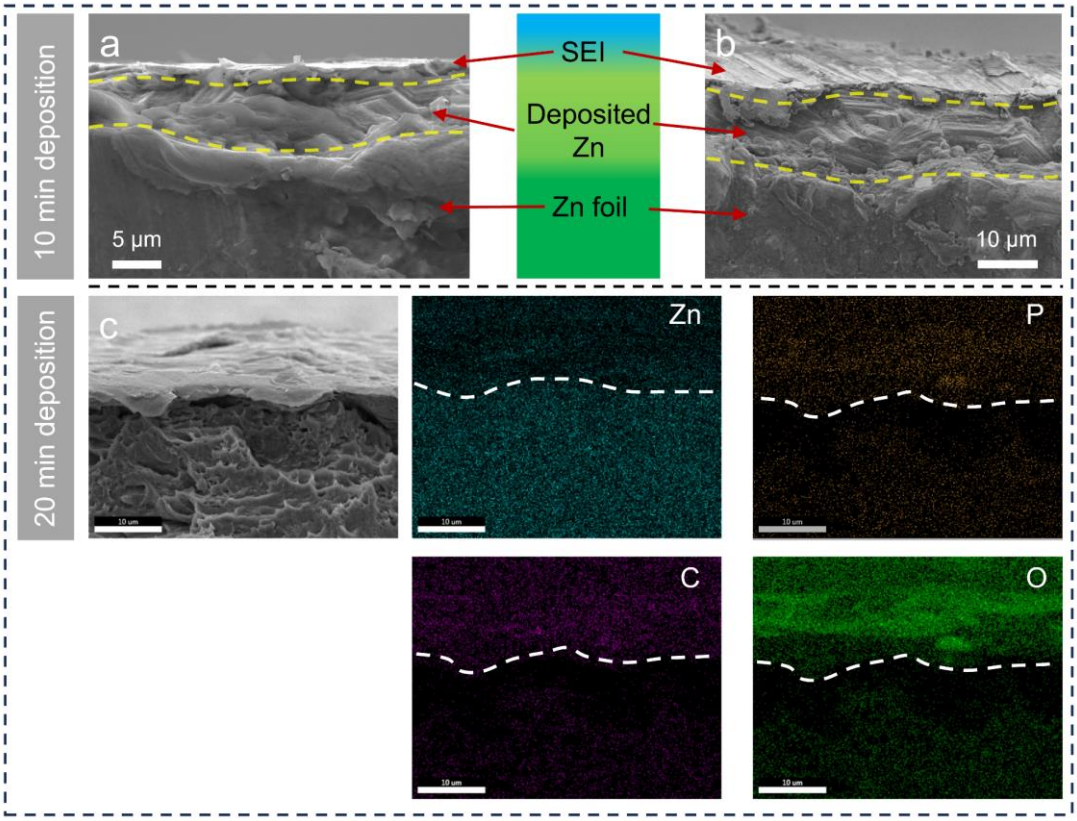

Supplementary Fig. 45 | Research on the electrochemical deposition behavior of SEI Zn electrode. (a, b) FESEM images of the side view of SEI Zn electrode deposited at a current density of 20 mA cm^{-2} for 10 minutes. (c) FESEM and corresponding EDS spectra of the side view of SEI Zn electrode deposited at a current density of 20 mA cm^{-2} for 20 minutes.

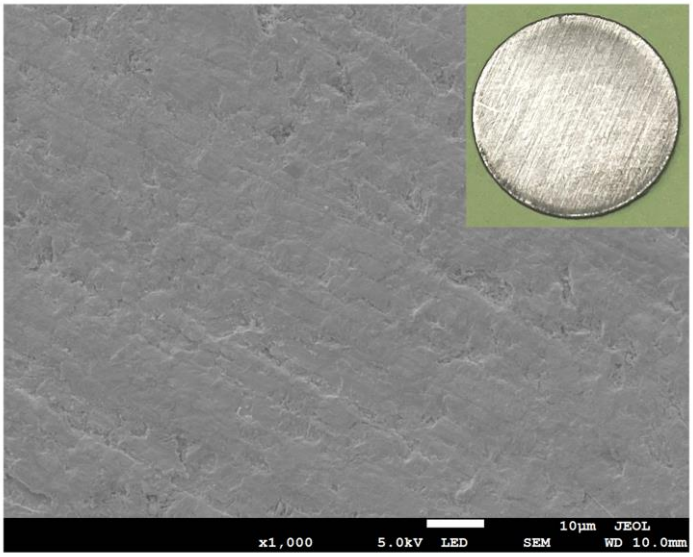

Supplementary Fig. 46 | FESEM images of SEI Zn electrode after 10 cycles.

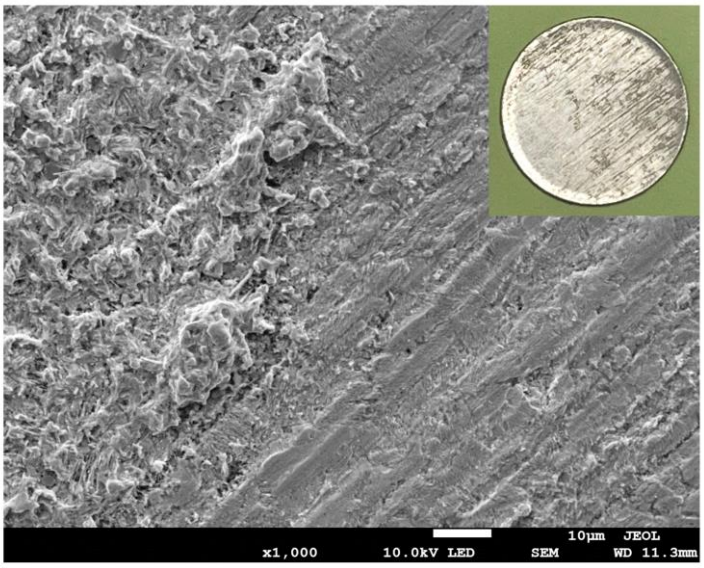

Supplementary Fig. 47 | FESEM images of Pure Zn electrode after 10 cycles.

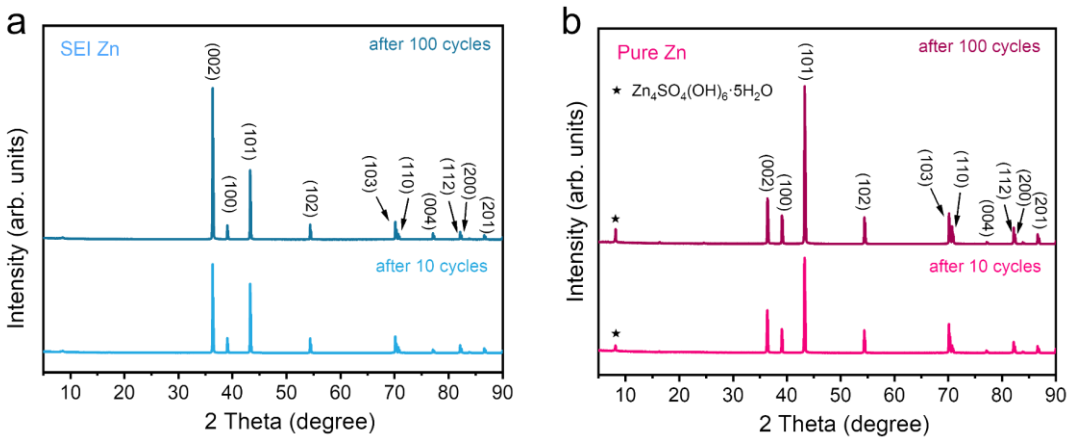

Supplementary Fig. 48 | The XRD patterns of (a) SEI Zn and (b) Pure Zn electrodes after different cycle number.

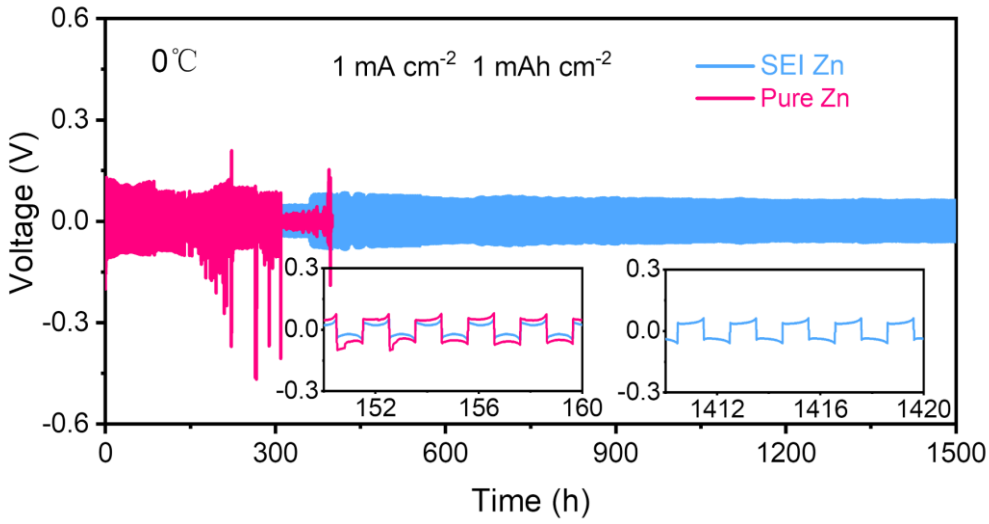

Supplementary Fig. 49 | Long-term cycle performance of pure Zn and SEI Zn electrodes at the condition of 1 mA cm^{-2} and 1 mAh cm^{-2} at 0°C.

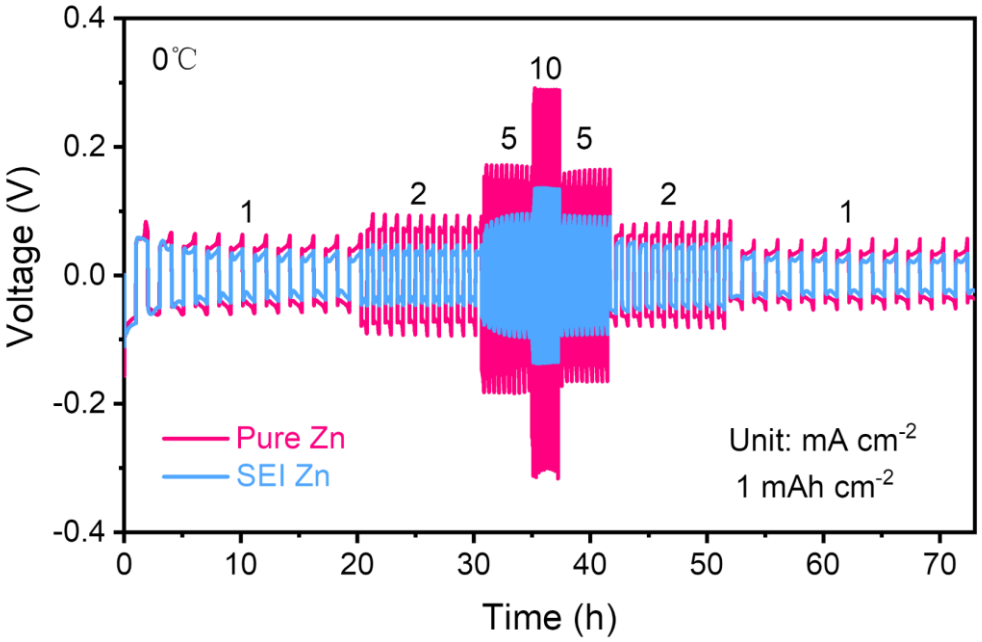

Supplementary Fig. 50 | Rate cycling performance test of pure Zn and SEI Zn electrodes at 0℃.

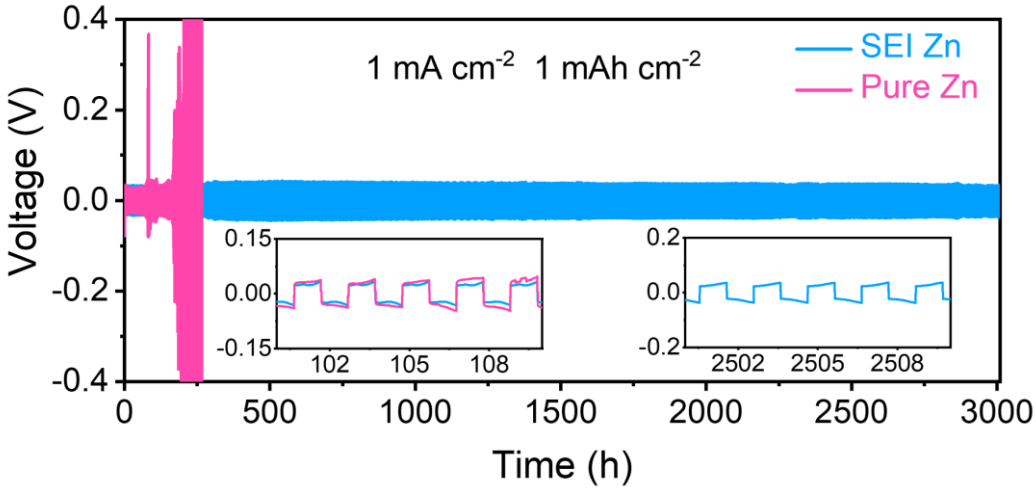

Supplementary Fig. 51 | Long-term cycle performance of pure Zn and SEI Zn electrodes at the condition of 1 mA cm^{-2} and 1 mAh cm^{-2} at 25℃.

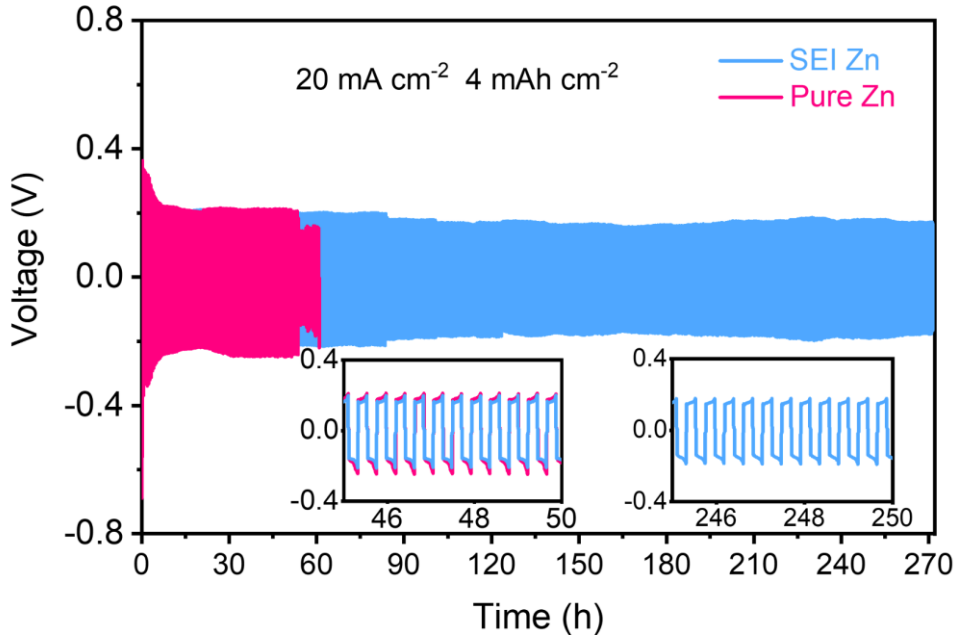

Supplementary Fig. 52 | Long-term cycle performance of pure Zn and SEI Zn electrodes at the condition of 20 mA cm^{-2} and 4 mAh cm^{-2} at 25℃.

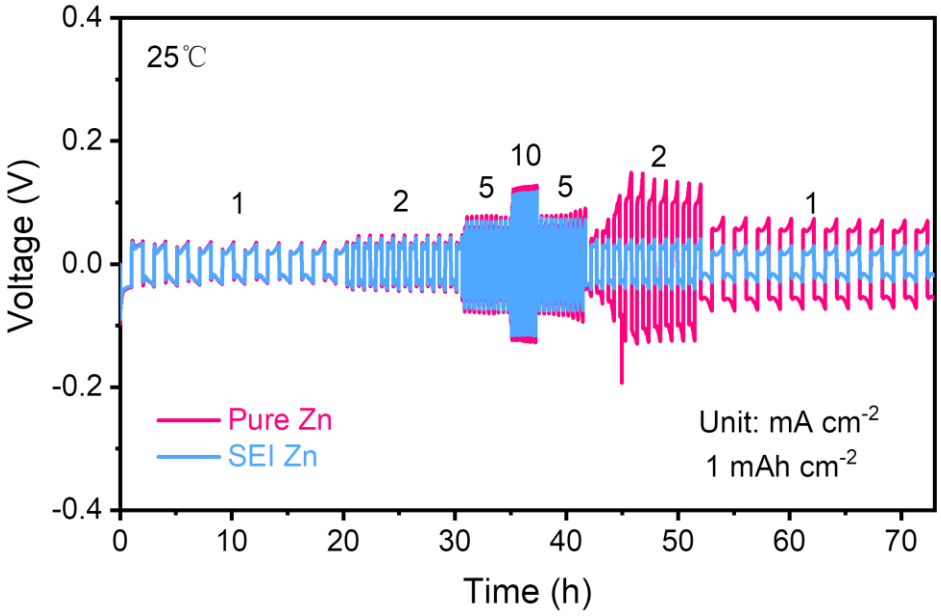

Supplementary Fig. 53 | Rate cycling performance test of pure Zn and SEI Zn electrodes at 25℃.

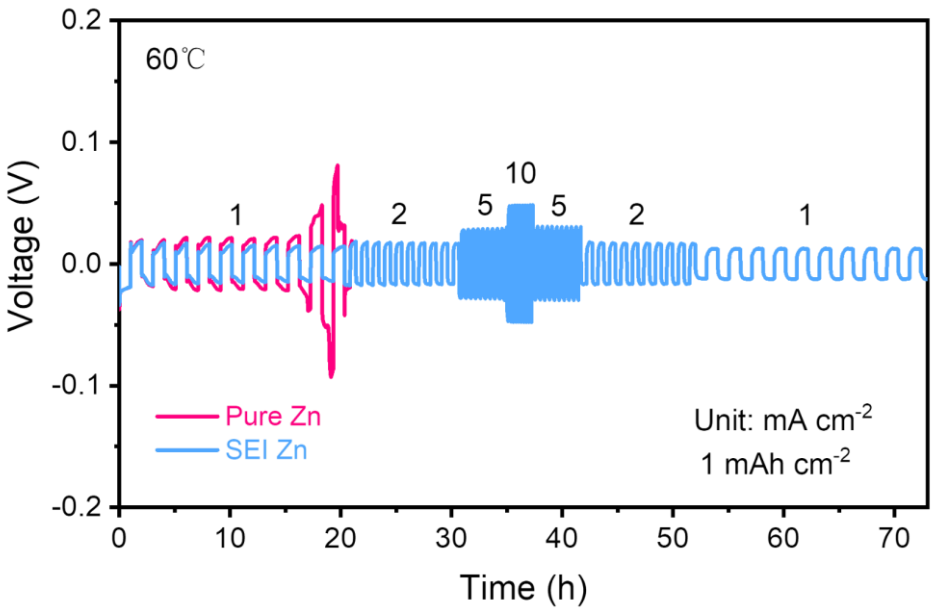

Supplementary Fig. 54 | Rate cycling performance test of pure Zn and SEI Zn electrodes at 60℃.

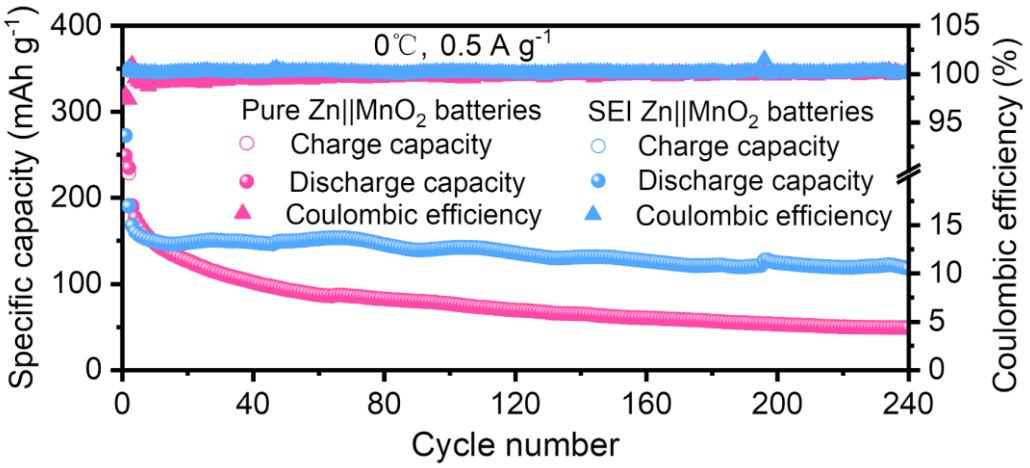

Supplementary Fig. 55 | The comparison of cycle stability of coin-type aqueous Zn||MnO_2 batteries at the current density of 0.5 A g^{-1}.

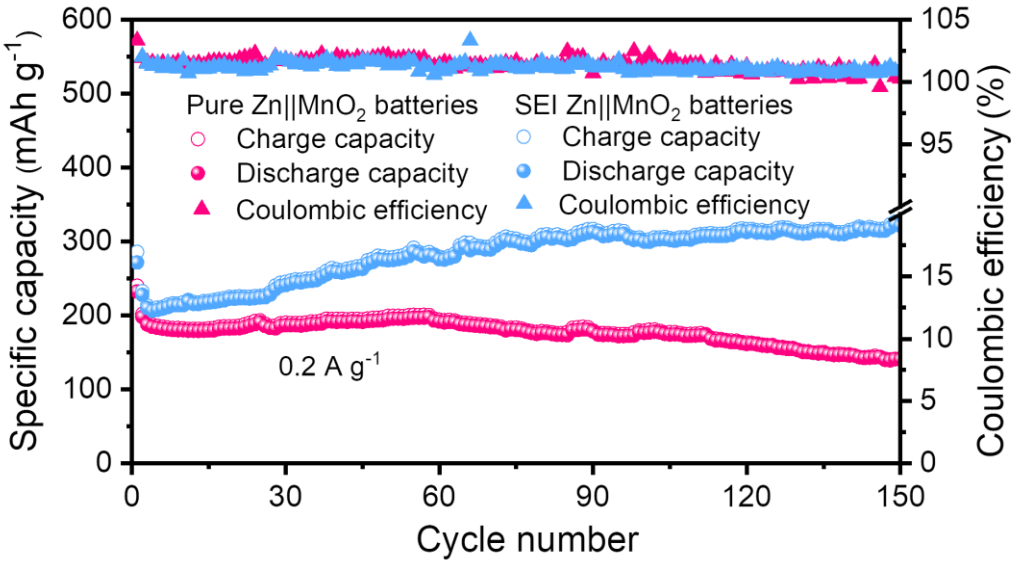

Supplementary Fig. 56 | The comparison of cycle stability of coin-type aqueous Zn||MnO_2 batteries at the current density of 0.2 A g^{-1}.

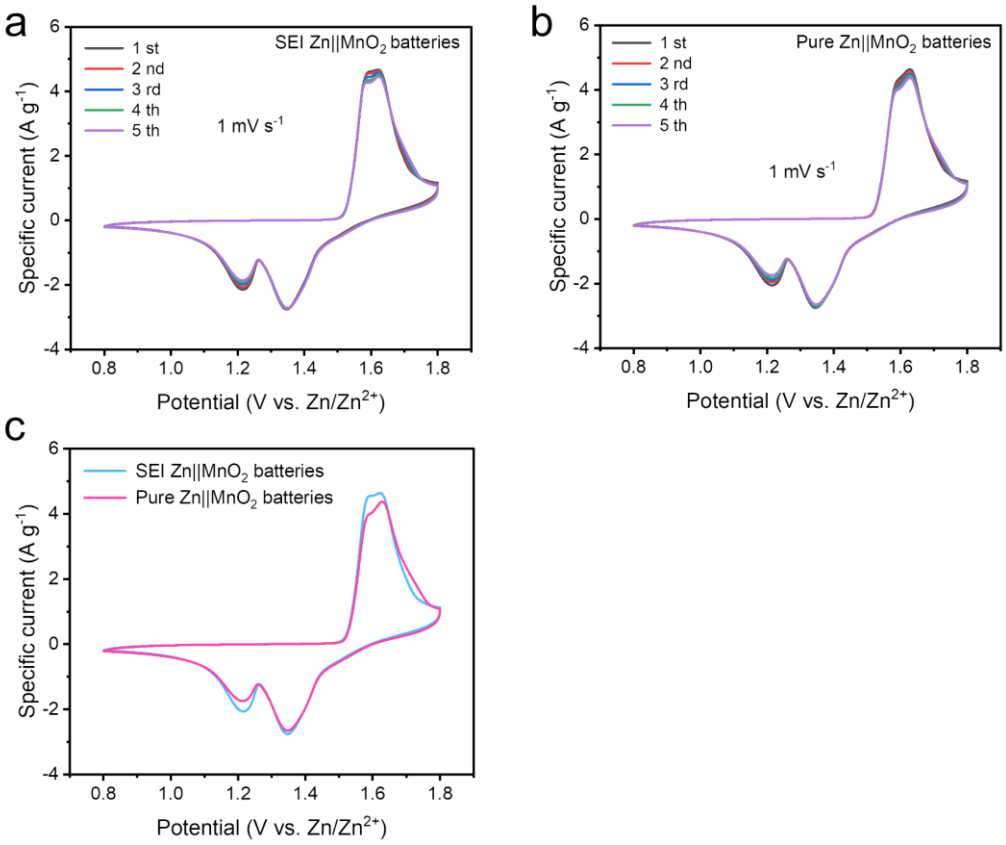

Supplementary Fig. 57 | Research on the electrochemical reaction behavior of Zn||MnO_2 batteries. The CV curves of coin-type Zn||MnO_2 batteries with (a) SEI Zn and (b) pure Zn negative electrodes in the initial 5 cycles at a scanning rate of 1 mV s^{-1}. (c) Their comparison of CV curves in the second cycle.

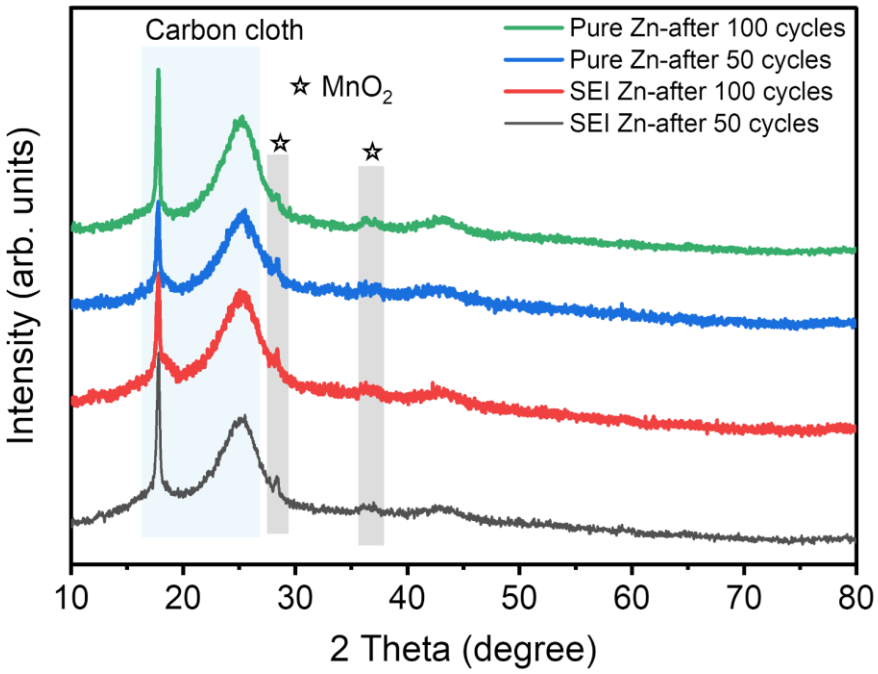

Supplementary Fig. 58 | XRD pattern of MnO_2 positive electrode after different cycles in the Pure Zn or SEI Zn negative electrode system.

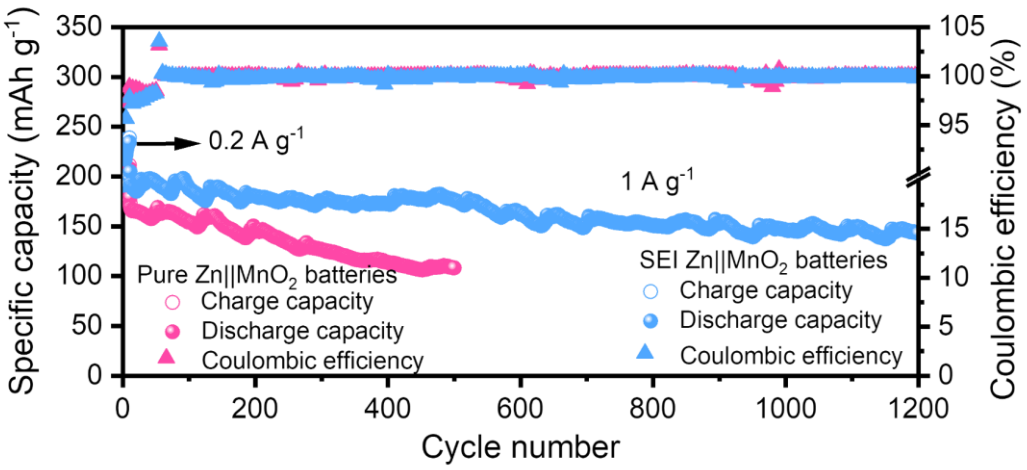

Supplementary Fig. 59 | Cycle performance test of the coin-type Zn||MnO_2 batteries in 3 M $ZnSO_4$ electrolyte and at the current density of 1 A g^{-1}.

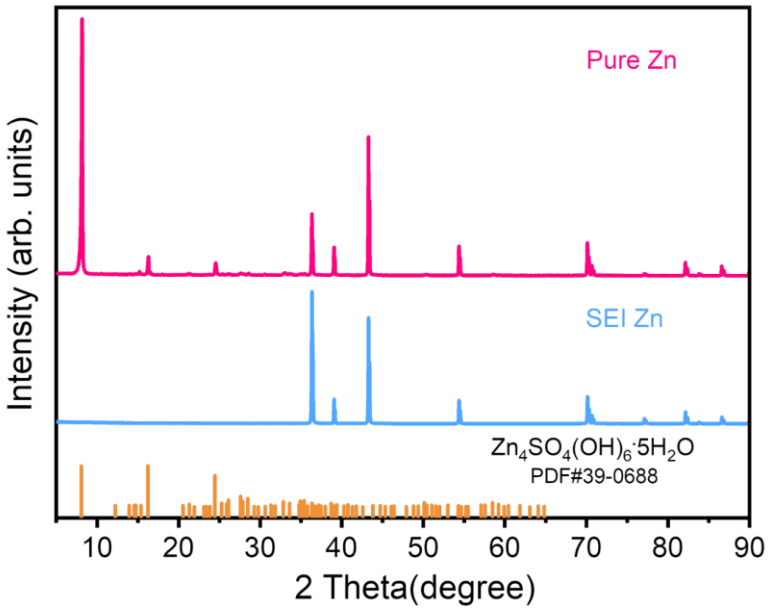

Supplementary Fig. 60 | XRD patterns of pure Zn and SEI Zn electrodes after different temperature cycles.

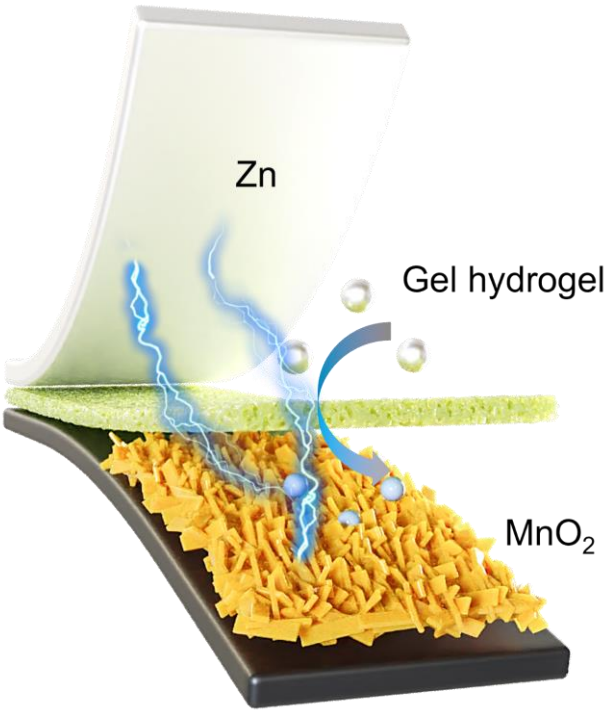

Supplementary Fig. 61 | The schematic diagram of flexible quasi-solid state SEI Zn||MnO_2 pouch cells.

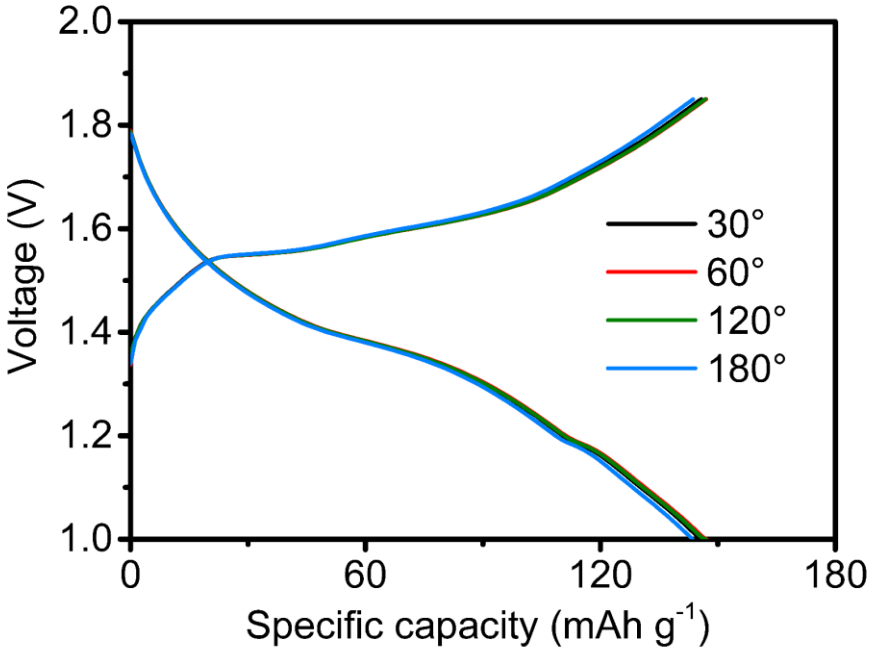

Supplementary Fig. 62 | Charge and discharge curves of flexible quasi-solid state SEI Zn||MnO_2 pouch cells bent at different angles.

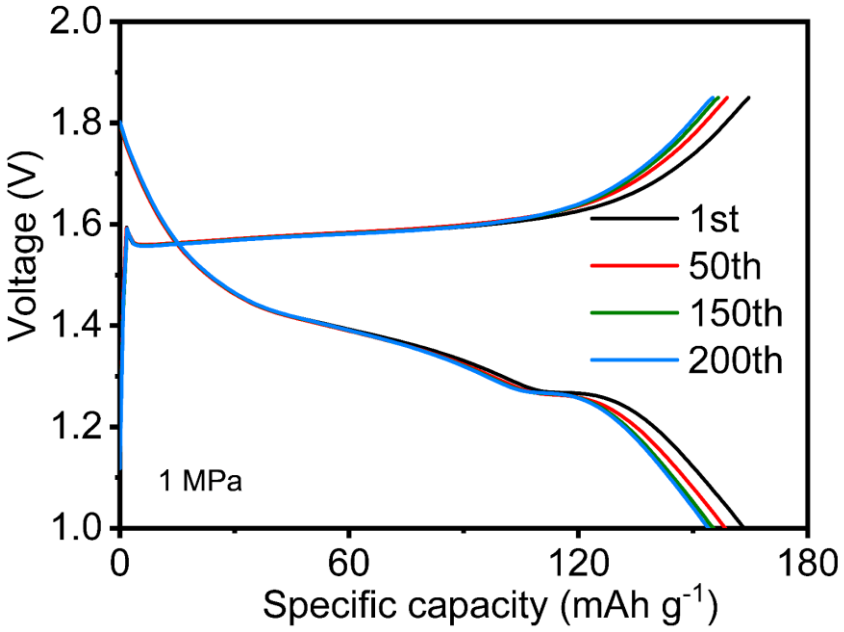

Supplementary Fig. 63 | Charge and discharge curves of quasi-solid state SEI Zn||MnO_2 pouch cells under high pressure (1 MPa) after different cycles.

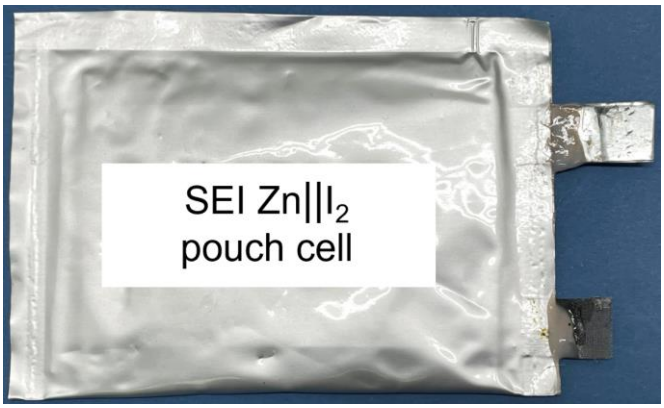

Supplementary Fig. 64 | Digital image of the assembled aqueous SEI Zn||I_2 pouch cell.

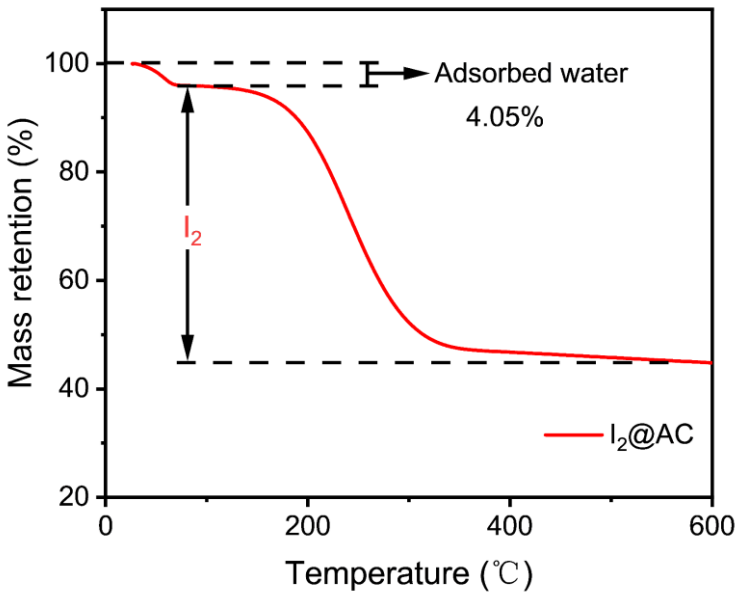

Supplementary Fig. 65 | TGA curve of the synthesized I_2@AC powder.

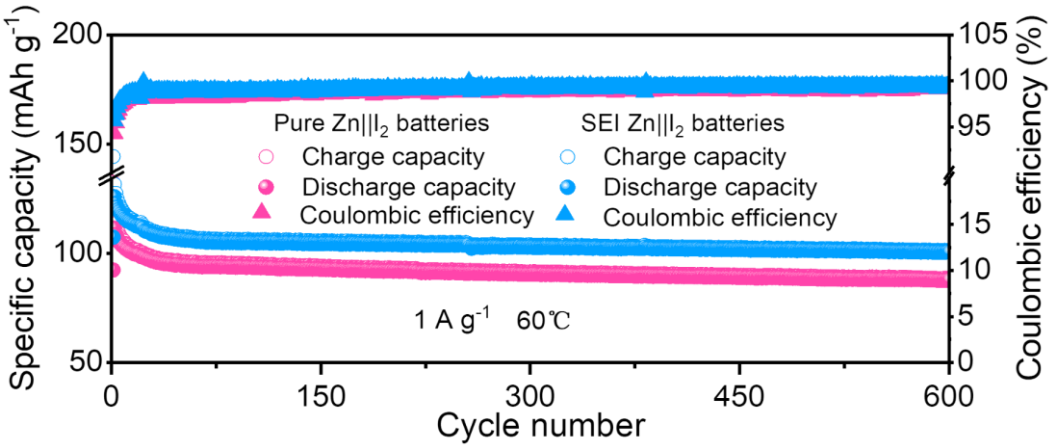

Supplementary Fig. 66 | The comparison of cycle stability of coin-type aqueous Zn||I_2 batteries at the current density of 1 A g^{-1} and at the temperature of 60℃.

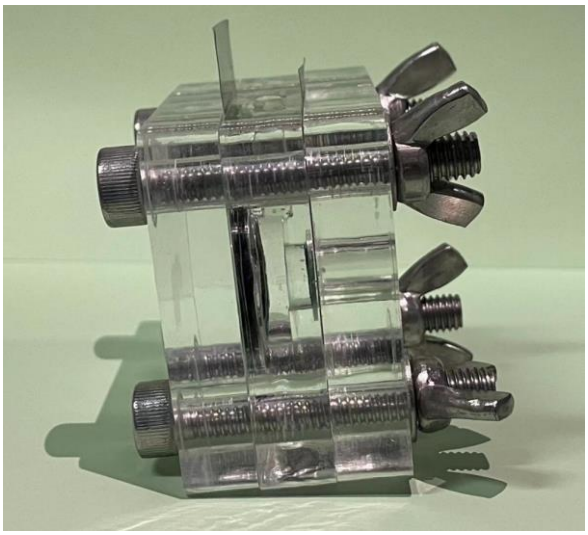

Supplementary Fig. 67 | Digital image of the assembled aqueous Zn-air batteries.

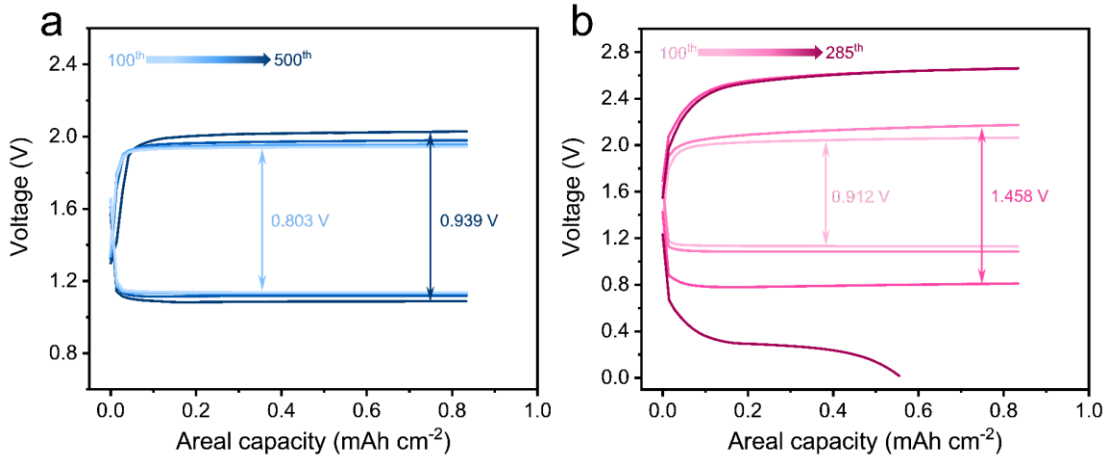

Supplementary Fig. 68 | Charge and discharge curves corresponding to long cycles of Zn-air batteries with (a) SEI Zn electrode, and (b) pure Zn electrode, respectively.

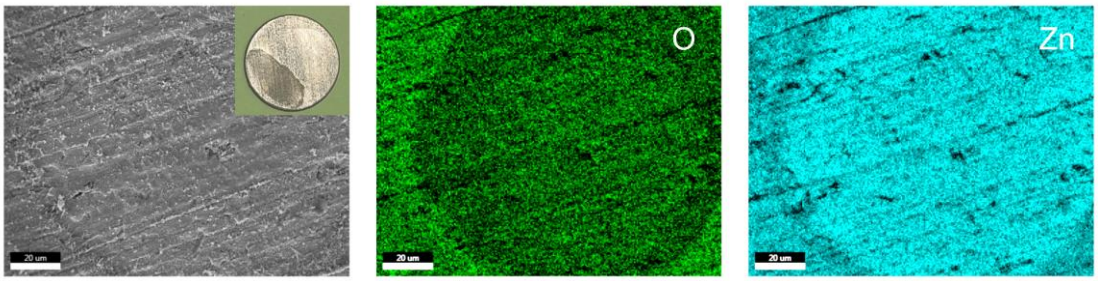

Supplementary Fig. 69 | Morphology and corresponding EDS images of pure Zn electrode soaked in KOH solution.

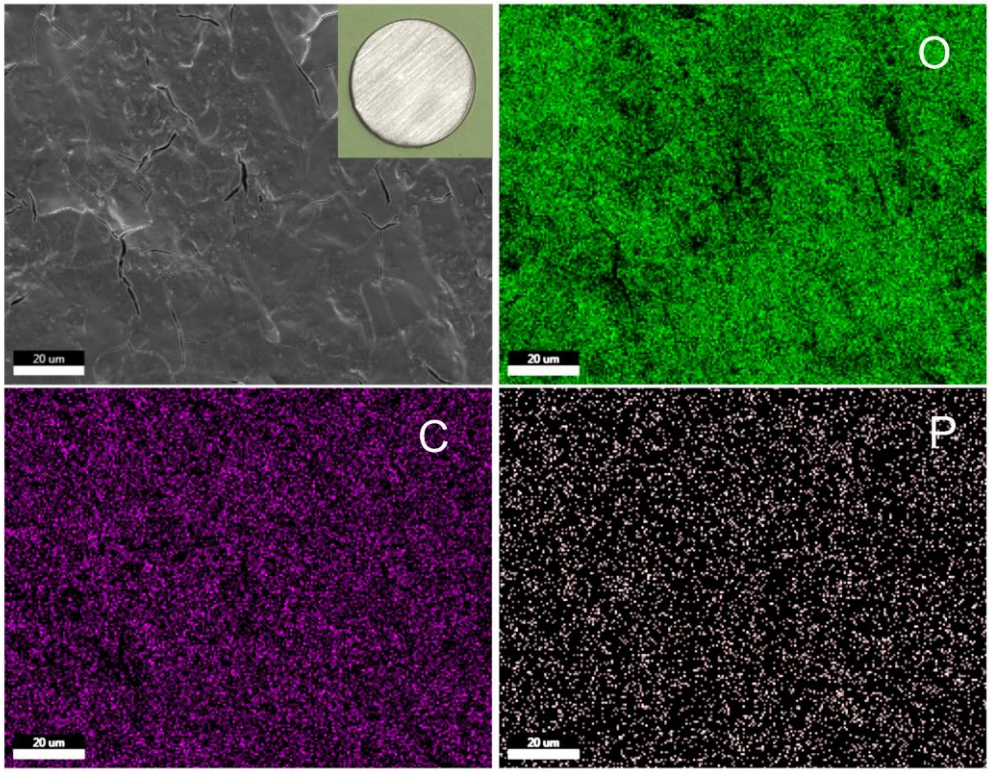

Supplementary Fig. 70 | Morphology and corresponding EDS images of SEI Zn electrode soaked in KOH solution.

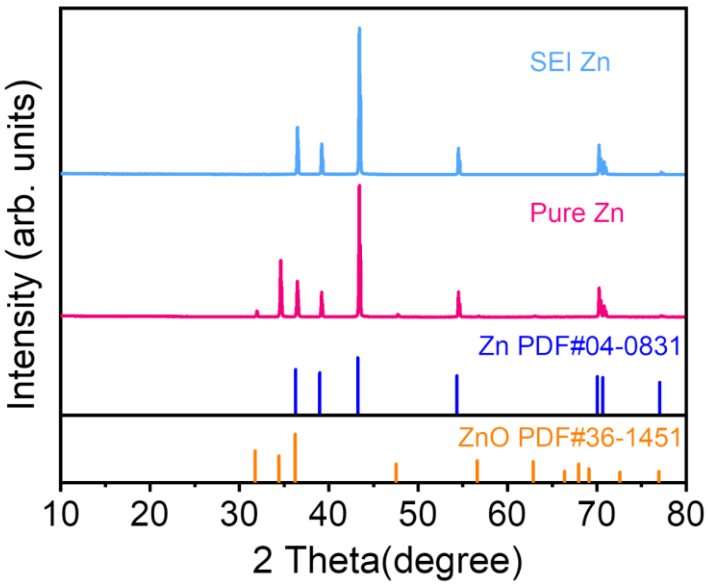

Supplementary Fig. 71 | XRD patterns of the pure Zn and SEI Zn electrodes after soaking in KOH solution.

Supplementary Table 1 | The fitted results of EIS test before and after polarization.

	Pure Zn		SEI Zn	
	before polarization	after polarization	before polarization	after polarization
R_{Ω} (Ω)	3.5±0.2	3.6±0.1	2.7±0.1	4.8±0.2
R_{ct} (Ω)	388.9±1.1	391.5±1.3	321.2±1.2	360.1±1.5

Supplementary Table 2 | The fitted results of EIS test at different temperatures.

	Pure Zn		SEI Zn	
Test temperature (°C)	R_{Ω} (Ω)	R_{ct} (Ω)	R_{Ω}(Ω)	R_{ct} (Ω)
30	2.5±1.4	366.5±1.4	2.0±0.3	242.3±1.5
40	1.8±1.1	202.3±1.1	1.6±0.2	186.5±1.2
50	1.5±0.3	130.2±1.3	1.4±0.4	124.5±1.6
60	1.3±0.1	81.2±1.6	1.2±0.3	96.7±1.1
70	1.1±0.2	65.2±1.2	0.9±0.1	64.6±1.3